# Advanced methodology for simulating local operating conditions in large fuel cells based on a spatially averaged pseudo-3D model

Marine Cornet, Jean-Philippe Poirot, Pascal Schott, Sebastien Kawka, Arnaud Morin, Yann Bultel

# Advanced methodology for simulating local operating conditions in large fuel cells based on a spatially averaged pseudo-3D model

## Authors

Marine Cornet[1], Jean-Philippe Poirot-Crouvezier[1,z], Pascal Schott[1], Sébastien Kawka[1], Arnaud Morin[1], Yann Bultel[2]

[1]*Univ. Grenoble Alpes, CEA, LITEN, DEHT, 38000 Grenoble, France*

[2]*Univ. Grenoble Alpes, Univ. Savoie Mont Blanc, CNRS, Grenoble INP, LEPMI, 38000 Grenoble, France*

*Corresponding e-mail: jean-philippe.poirot@cea.fr*

*Corresponding postal address: 17 avenue des Martyrs, 38000 Grenoble, France*

## Abstract

To address the performance and lifetime limitations of Proton Exchange Membrane Fuel Cells, it is essential to have a comprehensive understanding of the operating heterogeneities at the cell scale, requiring the test of a wide range of operating conditions. To avoid experimental constraints, numerical simulations seem to be the most viable option. Hence, there is a need for time-efficient and accurate cell-scale models. In this intention, previous works led to the development and the experimental calibration of a pseudo-3D model of a full-size cell in a stack. To further reduce the computation time, a new spatially averaged, multi-physics, single-phase, non-isothermal, steady state pseudo-3D model is developed and calibrated with the results of the preceding model. Particularly, it captures the influence of the coolant on temperature and water mappings in the cell. Moreover, a new methodology is proposed to calibrate the electrochemical cell voltage law for new membrane-electrode assemblies. The emulation of the local operation conditions in large active surface area is realized with a small differential cell, avoiding the testing of large single cells or stacks. Subsequently, simulations are conducted to investigate the impact of the coolant temperature gradient, coolant outlet temperature and gas relative humidity.

# Nomenclature

**Acronyms**

| | |
|---|---|
| 2D | Two-dimensional |
| 3D | Three-dimensional |
| MEA | Membrane Electrode Assembly |
| BL | Backing Layer |
| BP | Bipolar Plate |
| CCM | Catalyst Coated Membrane |
| CWC | Cooling Water Channel |
| CL | Catalyst Layer |
| CPU | Central Processing Unit |
| DOE | US Department of Energy |
| FCEV | Fuel Cell Electric Vehicle |
| GC | Gas Channel |
| GDL | Gas Diffusion Layer |
| MPL | Micro Porous Layer |

| | |
|---|---|
| OCV | Open Circuit Voltage |
| P3D | Pseudo-3D |
| PEM | Proton Exchange Membrane |
| RH | Relative Humidity |

**Latin**

| | | |
|---|---|---|
| $C_i$ | Correction factor | - |
| $c_p$ | Heat capacity | J/K |
| $E_{rev}$ | Reversible potential | V |
| F | Generic notation for a flux | - |
| | Faraday constant | C/mol |
| F | Generic notation for a flux density | - |
| h | Uniformity coefficient | - |
| $H_0$ | Enthalpy | J/mol |
| I | Identity tensor | - |
| i | Current density | A/cm² |
| $J_i$ | Species diffusion flux | kg/(m².s) |

| | | |
|---|---|---|
| $\sum J_i$ | Diffusive mass fluxes across the layers (P3D) | kg/(m².s) |
| $\sum J_e$ | Heat fluxes across the layers (P3D) | W |
| $K_1$ | Permeability | m² |
| $K_2$ | Passability coefficient | - |
| P p | Pressure | Pa |
| R | Universal gas constant | J/(K.mol) |
| $R_c$ | Contact resistance | Ω |
| $R_p$ | Protonic resistance | Ω |
| s | Standard deviation | - |
| $S_0$ | Entropy | J/(mol.K) |
| $S_m$ | Mass source term | kg/s |
| $S_i$ | Species source term | kg/s |
| T | Temperature | K or °C |
| $U_{cell}$ | Uniform cell voltage | V |
| $u$ | Local velocity | m/s |

| | | |
|---|---|---|
| $v$ | In-plane velocity | m/s |
| $w_i$ | Mass Fraction of the species i | - |

**Greek**

| | | |
|---|---|---|
| β | Empirical coefficient | - |
| ε | Porosity | - |
| $\eta_{ohm}$ | Over-potential | V |
| κ | Thermal conductivity | W/(m.K) |
| λ | Membrane water content | - |
| μ | Dynamic viscosity | Pa.s |
| ρ | Density | kg/m$^3$ |
| σ | Ionic conductivity | S/m |
| $\sum \phi_i$ | Through-plane convective fluxes | |
| $\sum \Phi_m$ | Through-plane mass fluxes | |
| Ω | Fluid flow cross-section | m² |

**Prefix**

a anode

c cathode

**Subscripts**

$CO_2$ carbon dioxide

$O_2$ oxygen

$H_2$ hydrogen

# 1. Introduction

Proton exchange membrane (PEM) fuel cells are a promising technology for transport with reduced $CO_2$ emissions. It is a particularly attractive option for heavy-duty vehicles in long-haul freight transportation because of its shorter refueling time and greater autonomy than batteries[1,2]. In fact, the global fuel cell vehicle (FCV) fleet increased from an estimated 13,000 vehicles in 2018 to 72,000 vehicles in 2022. The growth between 2020 and 2021 includes an increase of heavy-duty vehicles, as we go from a total of 852 in 2020 to 3321 in 2022[3]. Unfortunately, beyond the challenges of infrastructures and green hydrogen production, cost, performance and durability of PEMFC stack remain barriers to large-scale industrialization. The US Department of Energy (DOE) 2030 targets for long-haul heavy-duty fuel cell systems are $80/kW for the cost and 25 000 hours for lifespan[4].

To ensure better performance and durability of PEM stack, the management of the temperature, water content and current distributions at the cell scale is essential. In fact, the distributions over a large PEM fuel cell active surface area are subject to cross interactions, which makes operating heterogeneities a complex phenomenon to understand. Studies have highlighted key factors influencing the current density distribution, and therefore the performance of the cell. Indeed, limited performance due to liquid water obstruction (flooding) or decreased proton conductivity from membrane dehumidification (drying) might result from inefficient water and heat management of the cell[5,6,7,8]. Moreover, the designs of the gas distribution areas and channels of the bipolar plates play a role in the reactant distribution, so it affects performance as well[9,10,11,5]. Rodosik et al.[12] have also linked operating heterogeneities to local degradations, which affect the durability of the cell. One set of parameters that has yet to be investigated, with regard to its potential impact on heterogeneities, is the combination of the temperature gradient of the coolant, between the cell inlet and outlet, and its outlet temperature. The coolant gradient and outlet temperature play a key role regarding the optimization of the operation of a PEMFC system and its balance of plant (BOP). Indeed, a higher operational temperature, regulated by the coolant, enhance cell tolerance regarding CO poisoning, increase the efficiency of electrochemical reactions and water management[13–18]. With a higher operational temperature, the cell efficiency increases and the demand of cooling power decreases resulting in a better system efficiency. As the coolant absorbs heat along its

flow, the regions of the cell exhibiting the highest temperatures are near the coolant outlet. In practice, PEMFC systems are frequently regulated according to the coolant outlet temperature[19–21]. The operating temperature, which affects performance, is therefore directly linked to the coolant outlet temperature. Moreover, operating with a higher coolant temperature gradient through the cell could improve its operation at low gas relative humidity (RH), allowing a downsizing of the air humidifiers and hydrogen recirculation. A higher coolant temperature gradient would imply a reduction in coolant flow rate, which would mean downsizing the coolant pump. A significant number of studies, including experimental and numerical investigations, have already been conducted to examine the internal temperature characteristics of PEMFCs and their relationship to performance[11,17,18,22–30]. Indeed, the results of Yan et al.[31] showed that temperature has a considerable impact on the performance of PEM fuel cells, with a notable influence on membrane humidity and water transport within the gas diffusion layer and catalyst layer. Other studies show the critical impact of temperature and water distribution on the performance and durability of PEMFC[32,33]. Most numerical studies focus on testing different flow field or distribution area designs for the coolant channels to ensure uniform temperature distribution[34–38]. Nowadays, most PEMFC use multi-pass parallel flow field for the coolant[39]. However, these studies only look at the temperature distribution only at low power density or focus on making the temperature distribution as uniform as possible. A uniform temperature distribution is not achievable as the heat-flux caused by the electrochemical reactions varies spatially and an uncontrolled temperature distribution is not desirable. An uncontrolled temperature distribution can lead to the formation of hot spots and improper heat dissipation[40,41], as well as localized dehydration of the membrane, degradation of the membrane and, consequently, a detrimental impact on the performance of the PEMFC[33]. Liu et al.[42] studied the effect of the coolant inlet temperature by 1) keeping the coolant flow rate constant for three different coolant flow field designs and 2) varying the flow rate while keeping the coolant inlet temperature at 70 °C with a large-scale cell, non-isothermal and 3D model. However, as written previously, the regions of a cell exhibiting the highest temperatures are near the coolant outlet and PEMFC systems are usually regulated according to the coolant outlet temperature. None of the studies found by the authors has attempted to find a coolant temperature gradient, regulated on the coolant outlet temperature, which is optimal for performance and durability. Coolant flow is often fixed and non-optimized, in experimental testing, even during dynamic operation. It is, therefore, essential to study operating heterogeneities, giving due consideration to the influence of the coolant.

Experimental study of the operating heterogeneities, i.e. the current density and temperature distributions is possible thanks to segmented cell techniques: printed circuit board, resistors network and Hall effect sensors[43]. Maranzana et al.[8] have developed an experimental set-up for measuring two coupled quantities, current density and temperature, and for observing liquid water in the channels. Furthermore, water content distribution can be analyzed thanks to neutron imaging[44,45]. However, such methods may be invasive, or do not offer sufficient information about the water distribution and are

complicated to implement if several different bipolar plate designs are to be tested. In fact, several studies have attempted to model the results obtained using neutron imaging[46,47]. In addition, electrochemical systems are complicated to understand, analyze, develop and improve because of their multi-dimensionality, time-dependency, and the fact that many physics come into play. To go further in interpreting experimental results and test as many operating conditions as possible, a numerical approach seems to be the most appropriate, given the current computational capabilities that enable the simulation of coupled multi-physics models.

Since the first models by Springer et al.[18] and Bernardi and Verbrugge[17], many models for the study of PEMFC operation were developed. This includes models at all scales: from the pore scale to study the diffusion of reactants in porous component, to the scale of an entire cell and PEM stack, and from zero dimension to three dimensions (3D), passing through pseudo-2D and pseudo-3D (P3D). We can find steady state[48] or transient models[49–53], as well as single-phase or two-phase models[54–58]. Some models have even been developed as part of open source package like OpenFCST[59] or commercial packages, such as the Fuel Cell & Electrolyzer Module in COMSOL[60] and the Fuel Cell and Electrolysis module in ANSYS Fluent[61]. A comprehensive overview of models related to the operation of PEMFCs can be found in a number of reviews[62,63,55,64,65]. As of now, full 3D models are more accurate as they require fewer assumptions. However, 3D models are still costly in terms of calculation[66,64]. Zhang et al.[67] studied the current density distribution, for different flow field design, using a steady-state 3D model. The paper reports that ten thousand iterative steps are required for the simulations to converge, for active surface areas of 40 and 50 cm². Baca et al.[68] developed a single-phase 3D model to study the performance of PEM fuel cell under a few operating conditions. Depending on the operating conditions, it takes 4,000 to 8,000 iterative steps for the model to converge only at a rib/channel scale calculation domain (4 to 10hours of CPU time). The few relevant non-isothermal 3D models seen in the literature attempting to simulate large cells do not report the time and resources required for simulations[42,47]. However, this is an essential information for determining the applicability and usability of the models. Even with fewer limitations, regarding computational resources, computing time remains critical for large-scale studies with multi-dimensional models on the scale of a large cell. It requires improved methodology to reduce the iterations number and CPU time. Besides, most of the models found are isothermal and do not take into account the coolant physics[69–71]. Liu et al.[72] and Chen et al.[73] have integrated the coolant in their electrochemical model, however their models are based on a single straight channel and do not describe PEMFC in-plane heterogeneities.

Despite the availability of so many models and approaches, there is still a need for a multi-dimensional model with a reasonable computation time (no more than a day per operating condition) to easily carry out sensitivity studies. It should be adaptable to any size of active surface area, flow configuration (counter-flow or co-flow), BP design and input parameters (operating conditions and physical properties

of the cell components). This work is a new step towards a versatile, accurate and low time complexity model for the design of PEMFC, their understanding and improvement of performance and durability. The model presented in this paper is a spatially averaged, P3D model of a large PEM fuel cell (~250 cm²). It considers the cell as a superposition of layers, each layer being in-plane discretized to allow the observation of local heterogeneities over the Membrane Electrode Assembly (MEA) region. The transport equations are solved using a P3D approximation developed and implemented in a previous multi-physics and single-phase model by F. Nandjou et al.[74] and coupled to a semi-empirical electrochemical model for the current density prediction. Extending their work, we develop a new approach that allows significant reduction in computational time by spatially averaging the channels geometry over the active surface area. A comprehensive search of the literature revealed no instances of a 3D or P3D model with a comparable combination of simplification. We compare the simulation results obtained with the new spatially averaged P3D model with those obtained with the original P3D model for validation with an initial set of parameters, determined with MEAs having given GDLs and compositions of the active layers. Subsequently, in preparation for experimental validation with a more recent MEA formulation (new GDLs and different compositions of the active layers), we calibrate the electrochemical cell voltage law and change the model MEA input parameters. This calibration uses experimental data measured with a differential cell emulating the local operation condition on a large cell surface area. Finally, the fitted model is used to simulate over a hundred operating conditions with variation in coolant outlet temperature (from 60 °C to 80 °C), gas relative humidity (from 30 % to 60 %) and coolant temperature gradient (from 2 °C to 20 °C) between the inlet and the outlet.

In the following section 2, we describe the new spatially averaged P3D model by presenting the geometry, the conservation equations and the initial input parameters implemented in the model as well as the spatial averaging steps and electrochemical model implemented. In section 3, we describe the differential cell, the MEA formulation and the methodology used to calibrate the electrochemical cell voltage law. In section 4, we compare the simulation results of the original P3D model with those of the new spatially averaged P3D model for the initial MEA formulation. Simulation results obtained with the spatially averaged model after calibration are also presented to show the possibilities of investigation with this new model, namely, the influence of the water-cooling temperature gradient and outlet temperature.

# 2. Description of a new spatially averaged P3D model

## 2.1. Fuel cell geometry and inputs implemented

The cell design implemented in the model is a full-size PEM fuel cell with an active surface area of approximately 250 cm² with a length-to-width ratio of approximately 7/5. The bipolar plate design is an in-house design composed of two stamped stainless-steel sheets having a thickness of 100 µm. It

includes parallel-wavy channels for the anode fluid and for the cathode fluid, and the resulting cooling circuit. The dimensions of the channels are alike at the anode and cathode side, with a cross section area between 0.10 and 0.30 mm², identical rib-channel pitch in the range 1.0 – 1.5 mm and different channel depths. The geometry of the anode flow fields at the active surface area is shown in Figure 1 a). The full channel design is composed of a periodic sinusoidal-like elementary pattern with an amplitude/period ratio of 0.1 (Figure 1 b)).

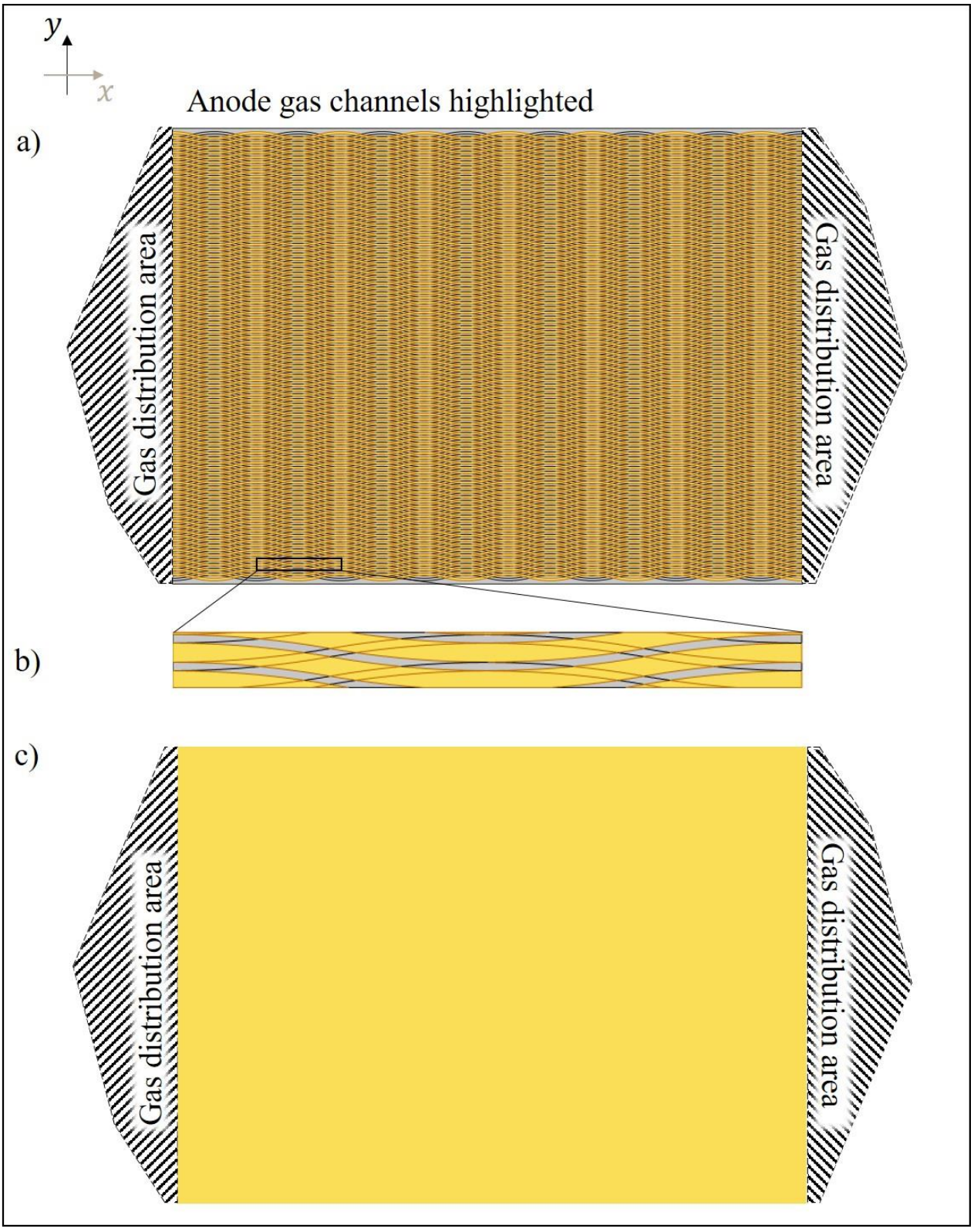


*Figure 1: a) Gas channels geometry implemented in the model with anode channels highlighted in yellow, b) the elementary patterns for the anode side and c) the entire spatially averaged active surface area.*

The gas distribution areas delimited on the right and left of the active surface area (Figure 1 a) and c)) are also implemented in the model. Their real design is not shown here for confidentiality reasons.

However, these areas are not spatially averaged unlike the active surface area. The gas distribution areas exert a significant influence on the distribution of gas on either side of the active surface area (air inlet and hydrogen inlet). Therefore, it is essential to be able to fully resolve the flow distribution at those specific locations. Despite the fact that these areas are designed to distribute gas in an optimal manner at the entrance to the active surface area, their design has a considerable impact on the heterogeneities observed along the y-axis.

The physical properties of the first MEA (MEA 1) used, including the membrane and the Catalyst Layer (CL), and the Gas Diffusion Layer (GDL), including the Backing Layer (BL) and the Microporous Layer (MPL), and initially implemented in the model is defined in Table 1. The physical properties values in Table 1 are issued from characteristics of commercial components found either in the literature, manufacturer's data or measurements performed at the CEA. However, as these parameters are used in a confidential project, it is not possible to give the references of the components or give more information on how the values were obtained.

| **Parameter** | **BP** | **GDL** | **CL (anode/cathode)** | **Membrane** |
|---|---|---|---|---|
| **Thickness (m)** | $1x10^{-4}$ | $1.74x10^{-4}$ | $6x10^{-6}/7.5x10^{-6}$ | $1.8x10^{-5}$ (dry) |
| **Thermal conductivity ($W.m^{-1}.K^{-1}$)** | 16.1 | In-plane: 6.1662<br>Through-plane: 0.353 | 1/1 | 0.186 |
| **Electric conductivity ($S.m^{-1}$)** | $13.5x10^{-5}$ | In-plane: 5747<br>Through-plane: 329 | 20/20 | |
| **Permeability ($m^2$)** | | In-plane: $1x10^{-12}$<br>Through-plane: $2.7x10^{-14}$ | $1x10^{-12}/1x10^{-12}$ | |
| **Tortuosity** | | In-plane: 1.74 | 3/3 | |

| | | | | |
|---|---|---|---|---|
| | | Through-plane: 1.13 | | |
| **Porosity** | | 0.76 | 0.47 | |
| **Average pore radius (m)** | | $\approx 1x10^{-5}$ | $\approx 1x10^{-8}$ | |
| **Platinum loading ($mg/cm^2$)** | | | 0.1/0.4 | |
| **Equivalent ionomer mass (kg/mol)** | | | | 0.735 |

*Table 1: Physical properties of the cell components implemented in both models.*

The values for GDL listed in Table 1 are the same at the anode and cathode. In the model, the BL and MPL form an effective GDL, which characteristics are taken into account for the resolution of the physics. However, for those components, we only have information on the GDL properties as a whole, indifferently from BL or MPL. The thickness values of the various layers are the uncompressed values provided by the manufacturers. Taking an average value between compressed and uncompressed GDL thickness could be an improvement for a future version of the model.

## 2.2. Spatial averaging methodology

The model used in this work is P3D. A detailed explanation of the P3D approach transition can be found in Refs.[75,74,76]. Briefly, a single PEM fuel cell at rib/channel scale can be represented as a 3D layered structure, a portion of which is shown in Figure 2 a).

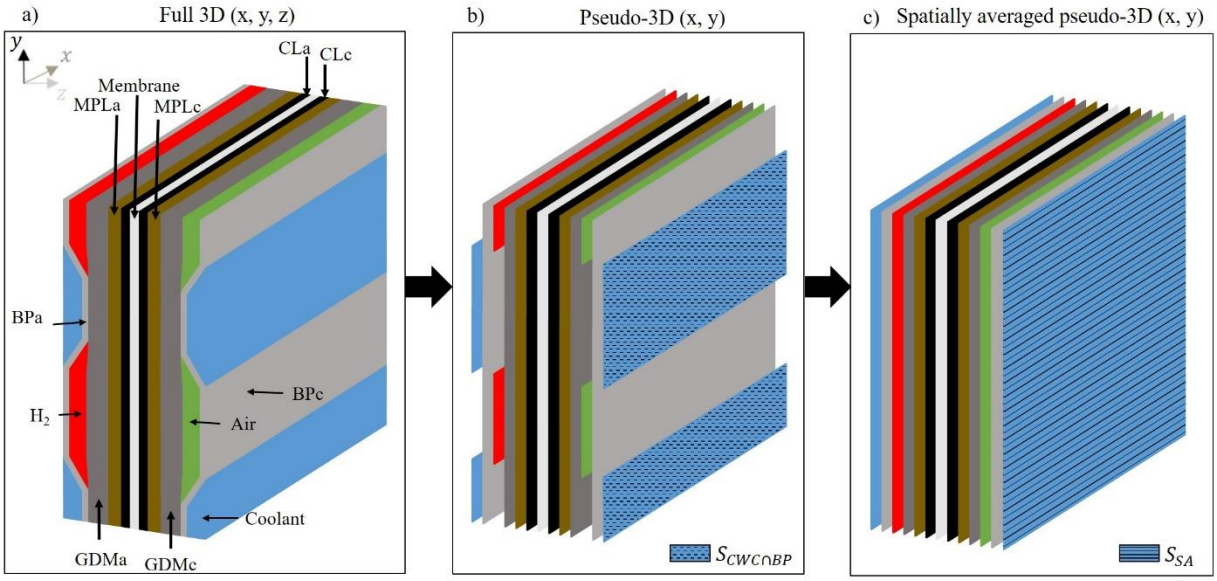


*Figure 2: 3D representation (a), P3D representation (b) and spatially averaged representation (c) of the cell at rib/channel scale*

It is composed of a proton exchange membrane in the center, sandwiched between the electrodes, one anode and one cathode, each made of a catalyst layer. They are named CLa and CLc in the model for the anode and cathode side respectively. To ensure the diffusion of the reactant, the membrane electrode assembly (MEA) is enclosed between two GDLs composed of a carbon fiber support, also called backing layer (BL), and a microporous layer (MPL). Similarly, the anode-side GDL is called GDLa and the cathode-side GDL is called GDLc in the model. Finally, two metal bipolar plates surround these central layers. They allow the cell to be supplied with reactants and to cool the cell through channels for gas at the anode (GCa) and at the cathode (GCc), and coolant (CWC). Moreover, the bipolar plates collect the current and heat produced. The metal layers of the bipolar plates are called BPa and BPc in the models for the stamped metal sheets of the anode and cathode sides respectively.

The thickness of the cell is small compared to its length and width: the aspect ratio between the thickness and the length or the width ($\frac{Cell\ thickness}{Cell\ width}$) is usually between $1x10^{-5}$ and $1x10^{-2}$ [76]. So, each 3D layer can be reasonably approximated as a 2D in-plane layer. The assembly of the in-plane layers forms the initial P3D representation of the cell (Figure 2 b)). It should be noted that, in that initial case, the 2D in-plane layers corresponding to fluid media in channels (GCa, GCc and CWC) form discontinuous surfaces, as each fluid is present only at the location of the channels and not in front of the ribs.

The classical 3D conservation equations for fluid circulation layers (GCa, GCc, CWC, GDLa, GDLc, CLa and CLc), presented in Table 2, are integrated over the layer's thickness to obtain 2D in-plane conservation equations including inter-layer/cross-layer source terms for diffusion and/or convection fluxes (Table 2 column 3).

| | Full 3D conservation equations in stationary state **(domain of application)** | P3D conservation equations in stationary state **(domain of application)** |
|---|---|---|
| Continuity | $\vec{\nabla} \cdot (\rho\vec{u}) = S_m$ **(GC, GDL, CL and CWC)** (1) | $\nabla \cdot (\rho\vec{v}) = S_m + \sum \Phi_m$ **(GC, GDL, CL and CWC)** (2) |
| Species | $\nabla \cdot (\rho w_i \vec{u}) = -\nabla \cdot J_i + S_i$ **(GC, GDL and CL)** (3) | $\nabla \cdot (\rho w_i \vec{v}) = -\nabla \cdot J_i + \sum \phi_i + \sum J_i + S_i$ **(GC, GDL and CL)** (4) |
| Energy | $\rho c_p \vec{u} \cdot \nabla T = \nabla \cdot (\kappa \nabla T) + Se$ **(GC, GDL, CL and CWC)** (5) | $\rho c_p \vec{v} \cdot \nabla T = \nabla \cdot (\kappa \nabla T) + \sum J_e + Se$ **(GC, GDL, CL and CWC)** (6) |
| Momentum | $\frac{\rho}{\varepsilon}(\vec{u} \cdot \nabla)\frac{\vec{u}}{\varepsilon} + \nabla p = \nabla[\frac{1}{\varepsilon}(\mu\left(\nabla\vec{u} + (\nabla\vec{u})^T - \frac{2}{3}\mu(\nabla \cdot \vec{u}) \cdot I\right] - \left(\frac{\mu}{K_1} + \frac{S_m}{\varepsilon^2}\right)\vec{u} + \rho g$ **(GDL and CL)** (7) | $\nabla p = -u_z \frac{\mu}{K_1}$ **(GC, GDL and CL)** (8) |
| | $\rho(\vec{u} \cdot \nabla)\vec{u} + \nabla p = \nabla[\mu\left(\nabla\vec{u} + (\nabla\vec{u})^T - \frac{2}{3}\mu(\nabla \cdot \vec{u}) \cdot I\right] + \rho g$ **(GC and CW)** (9) | $\nabla p = \frac{1}{K_1}\mu\vec{v} + \frac{1}{K_2}\|\vec{v}\|\vec{v}$ **(CWC)** (10) |

*Table 2: Governing equations from 3D to P3D (application domains specified in bold)*

In all the equations, $\vec{u}(x,y,z) = u_x\vec{\imath} + u_y\vec{\jmath} + u_z\vec{k}$ is the local fluid velocity, $\vec{v}(x,y) = u_x\vec{\imath} + u_y\vec{\jmath}$ is the in-plane fluid velocity and $u_z$ is the through-plane fluid velocity. Moreover, $T$, $p$, $\rho$, $\mu$, $\varepsilon$, $K_1$, $c_p$ and $\kappa$ are, respectively, the mean temperature and pressure along the thickness of the component, the mixture density and the dynamic viscosity of the fluid, the porosity, the permeability, the heat capacity and the thermal conductivity of the component. In the 3D and 2D in-plane continuity equations, $S_m$ is the mass source term along the thickness of the component. In the 2D in-plane continuity equation, $\sum \Phi_m$ are through-plane mass fluxes exchanged between one given component and the adjacent ones. In the species conservation equations, $J_i$, $S_i$ and $\rho w_i$ are, respectively, the species diffusion flux, the local species source term and the mean species concentration along the thickness of the component. In the 2D

in-plane species conservation equation, $\sum \phi_i$ are the through-plane convective fluxes and $\sum J_i$ are the through-plane diffusive fluxes. In the energy conservation equations, $S_e$ is the local heat source. $\sum J_e$ is the sum of the through-plane heat fluxes in the 2D in-plane energy conservation equation. Then, in the 3D momentum equations, $\frac{2}{3}\mu(\nabla \cdot \vec{u}) \cdot I$ is the isotropic stress tensor. Lastly, regarding the 2D in-plane momentum equations, the Darcy's law is used in the gas channels and the Darcy-Forcheimer's law in the cooling channels. In fact, the channels are treated as a porous medium to simplify the calculation, reducing the number of solved variables. This analogy has already been used by several studies[77] [78] [56] [79] [54], and is based on the assumption that the flow inside the channel is laminar and that the relation between pressure drop and fluid velocity is linear. In the 2D in-plane momentum equations $K_2$ is the passability coefficients, which accounts for the pressure drops due to section and direction variations. It depends on $K_1$ and is defined as:

$$K_2 = \frac{\alpha \times \rho_{CW}}{\sqrt{K_1}} \tag{11}$$

where α is an empirical quadratic term and $\rho_{CW}$ is the density of cooling water.

The model presented in this work is not only P3D but also spatially averaged. The focus of our work being the operating heterogeneities, we have developed a method allowing to simplify the detailed fluid flow field geometries (GCa, GCc and CWC) (Figure 2 c)). In the initial P3D method, the active area of the cell is composed of a patchwork of different elementary areas, distributed over the whole surface. Four cases are encountered: anode land facing cathode land or cathode channel, and anode channel facing cathode land or cathode channel. This leads to the description of a discontinuous surface, imposing the use of a fine mesh (Figure 1 a)). Nevertheless, an elementary surface containing these four types of surfaces following a periodic pattern can be extracted (Figure 1 b)). The transport properties are then homogenized over this elementary surface. As a result, the flow fields become continuous surfaces over the entire active area (Figure 2 c)), where a much simpler mesh can be used (Figure 1 c)). This simplification allows to reduce significantly the computation time. As the flow fields are now continuous, the fluids can pass over the entire active surface area. To preserve the values calculated using the initial 2D in-plane equations (Table 2 column 3), despite spatially averaging the geometry, the method imposes several corrections. The equations implemented in the new spatially averaged model for fluid circulation layers (GCa, GCc, CWC, GDLa, GDLc, CLa and CLc) are therefore the 2D in-plane equations in the third column of Table 2, with corrections to the exchanges fluxes and the channel layers (GC and CWC) permeability. We describe the corrections made for spatially averaging the model in the following paragraphs.

The channels are considered as porous medium with a porosity of 1 and a certain permeability ($K_1$). In the case of the detailed geometry, the fluids pass through the cross-sectional area of the channels ($\Omega$). By averaging the channel geometries in the spatially averaged model, the same fluids pass through the "spatially averaged cross-sectional area" ($\Omega_{SA}$), calculated by multiplying the width of the active surface area (y-axis) and the thickness of the layer (z-axis). Transitioning from a detailed to a spatially averaged geometry, mass and momentum conservation at the cell scale in GC and CWC (Eq. (8) and Eq. (10)) must use an effective anisotropic permeability, which is referred to as $K_{1_{SA}}$. The latter can be expressed as a function of the permeability $K_1$ of the detailed geometry and a correction factor ($C_{K_1}$). $C_{K_1}$ is calculated by dividing the fluid flow cross-sectional area of the detailed geometry ($\Omega$), by fluid flow cross-sectional area of the spatially averaged geometry ($\Omega_{SA}$).

$$K_{1_{SA}} = K_1 \times \frac{\Omega}{\Omega_{SA}} = K_1 \times C_{K_1} \tag{12}$$

The anisotropic permeability of all channel medium (GCa, GCc and CWC) are calculated in this manner. We can therefore rewrite Eq. (8) with the anisotropic permeability ($K_{1_{SA}}$) for the GCs (Eq. (13)) and Eq. (10) with the anisotropic permeability ($K_{1_{SA}}$) and anisotropic passability coefficient ($K_{2_{SA}}$) for CWC (Eq. (14)).

$$\nabla p = -\vec{v}\frac{\mu}{K_{1_{SA}}} \textbf{ (GC)} \tag{13}$$

$$\nabla p = \frac{1}{K_{1_{SA}}}\mu\vec{v} + \frac{1}{K_{2_{SA}}}\|\vec{v}\|\vec{v} \textbf{ (CWC)} \tag{14}$$

In the case of the detailed geometry, the diffusive flux from the gas channel to the catalyst layer, across the GDL (GC∩GDL), is affected by the presence of ribs as shown in Figure 3. Two zones appear, each one having a different configuration of the fluid flow. In front of the channel, it can be considered that the gas flows directly along line segments of length ($l$). The latter is constant and equal to the GDL thickness. In front of the rib, the gas follows longer paths, starting from the edge of the channel and reaching the catalyst layer at every coordinate ($y$) along line segments of length ($l'$), calculated using ($l$) and ($y$).

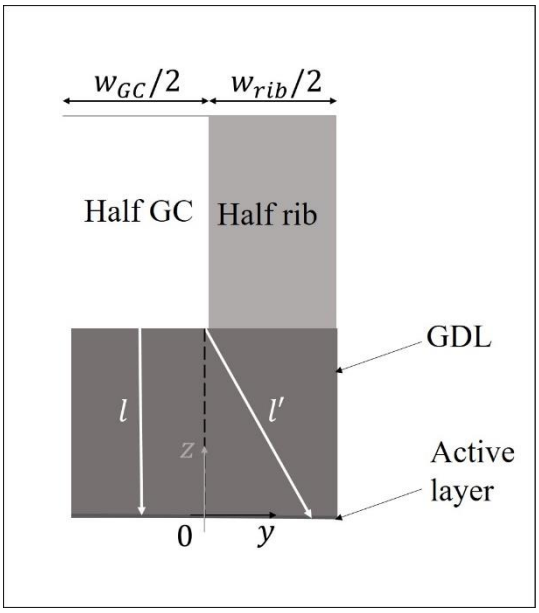


*Figure 3: Schematic representation of fluid diffusion in the GDL for a cross section of the rib, channel and GDL in the case of the detailed geometry of the P3D model*

In the spatially averaged approach, channels and ribs are not differentiated. Based on the above description of the flow in front of the channel and the rib, one unique equivalent fluid path length ($l_{SA}$) can therefore be expressed as a function of ($l$), ($l'$), ($y$), the width of a gas channel ($w_{GC}$), the width of a rib ($w_{rib}$).

$$l_{SA} = \frac{\int_{-w_{GC}/2}^{0} l dy + \int_{0}^{w_{rib}/2} \sqrt{l^2 + y^2} dy}{(w_{GC} + w_{rib})/2} \tag{15}$$

Both GDL thickness, being used in the solving of other physics in the model, and the total path length of the diffusive flux have to be preserved when we average the geometrical description in the model. Therefore, we correct the tortuosity of the GDL (in thickness and in plane) on both sides (anode and cathode) by introducing a purely geometric factor ($C_{tor}$) :

$$\tau_{SA} = \tau_{GDM} \times \frac{l_{SA}}{l} = \tau \times C_{tor} \tag{16}$$

This change in GDL tortuosity is a first correction of the diffusive flux densities and the convective flux densities exchanged between the GC and the GDL (GC∩GDL) and between the GDL and the CL (GDL∩CL), in order to preserve the values of $\sum \phi_i$ and $\sum J_i$ in Eq. (4), despite spatially averaging the geometry.

The applied 2D in-plane conservation equations (Table 2) include terms for fluxes exchanged at the intersection of two layers A and B, which are referred to as cross-layer fluxes and denoted as F in this paragraph. Transitioning from a detailed to a spatially averaged geometry means that the exchange surfaces of these fluxes change (example for the CWC in Figure 2 b) and c)). We go from an exchange surface denoted as $S_{A\cap B}$ for the detailed geometry to an exchange surface denoted as $S_{SA}$ for the spatially averaged geometry. To maintain the fluxes conservation, it is necessary to correct the corresponding flux densities values, noted f, using a correction factor ($C_f$). The correction factor is calculated by dividing the exchange surface in the detailed geometry ($S_{A\cap B}$) by the exchange surface in the spatially averaged geometry ($S_{SA}$). The corrected flux density ($\mathrm{f}_{SA}$) can be expressed as follows.

$$\mathrm{f}_{SA} = \mathrm{f} \times \frac{S_{A\cap B}}{S_{SA}} = \mathrm{f} \times \mathrm{C}_f \tag{17}$$

Table 3 lists all the flux densities corrected in this manner and the intersections of the domains where these fluxes are exchanged. For instance, a heat flux is exchanged between the coolant and the BP (CWC∩BP) at the contact surface between these two layers represented in Figure 2 b) ($S_{CWC\cap BP}$).

| Type of flux density | Intersections of flux exchange layers |
|---|---|
| Heat | GC∩GDL; GC∩BP; GDL∩BP; CWC∩BP; BPa∩BPc; |
| Electric | BPa∩BPc; MEA∩Rib |
| Convective | GC∩MEA |
| Diffusion | GC∩MEA |

*Table 3: Summary of cross-layers fluxes corrected for the spatially averaged model*

This correction makes it possible to conserve the value of $\sum J_e$ in Eq. (6). This is also the second correction made to flux densities in order to preserve the value of $\sum J_i$ and $\sum \phi_i$ in Eq. (4). Finally, the electric flux densities corrected in that manner are calculated using the electrochemical model developed in the next sub-section.

## 2.3. Water management, gas crossover and electrochemical cell voltage law

As, the model is single-phase, the simulated water is considered as an incondensable and ideal gas. Therefore, liquid and gas phases are assimilated to water vapor, with a pressure that can be higher than the saturation pressure. In the case of the water pressure being higher than the saturation pressure, we can assume that liquid water should be present and circulating. Therefore, the relative humidity calculated may be higher than 100%, which is synonymous with a theoretical presence of liquid water. This hypothesis implies that the water activity $a$ can be higher than 1. It is expressed by Springer et al.[18] as:

$$a = \frac{P_w}{P_{sat}} \tag{18}$$

where $P_w$ is the partial pressure of water, which can exceed the saturation pressure $P_{sat}$. As a result, a water content (average number of water molecules per sulfonic site) λ higher than 14 can be reached, using the expression from Springer et al.[18].

$$\lambda(a) = \begin{cases} 0.043 + 17.81 \times a - 39.85 \times a^2 + 36^3 \; if \; a \leq 1 \\ 14 + 1.4(a-1) \qquad\qquad\qquad\qquad if \; a > 1 \end{cases} \tag{19}$$

The upper limit for the water content is set at 22, corresponding to a complete water saturation of the membrane, which is obtained when the membrane is in contact with liquid water.

In the model, the water transport through the membrane is implemented by considering Electro-osmotic drag (EOD) and diffusion. The hydraulic permeation is considered negligible compared to the two phenomena mentioned. The flux of EOD is defined as:

$$J_{EOD} = \frac{a_{EOD} \times M_{H_2O}}{F} \times i \tag{20}$$

where $F$ is the Faraday constant and $a_{EOD}$ is the electro-osmotic drag coefficients and defined with the Meier et al.[80] approach in the model as:

$$a_{EOD} = 1 + 0.028 \times \lambda + 0.0026 \times \lambda^2 \tag{21}$$

As for the diffusion, we consider the Fick's law to describe the diffusive flux density as:

$$J_{diff} = D_M \times \frac{M_{H_2O}}{e_{MB}} \times c_f \times (\lambda_{CL_a} - \lambda_{CL_c}) \tag{22}$$

where $e_{MB}$ is the membrane thickness, $c_f$ is the molar concentration of sulfonate sites in the membrane, $\lambda_{CL_a}$ and $\lambda_{CL_c}$ are the water contents at the interfaces between the membrane and anode/cathode catalyst pores, respectively. $\lambda_{CL_a}$ and $\lambda_{CL_c}$ are calculated using Eq. (19). Finally, $D_M$ is the membrane water diffusivity, which is defined with Zawodzinski et al.[81] approach and is defined as:

$$D_M = (6.707 \times 10^{-8} \times \lambda_{MB} + 6.387 \times 10^{-7}) \times e^{(-\frac{2416}{T})} \tag{23}$$

Where the membrane water content, $\lambda_{MB}$, is calculated by a water mass balance in the membrane taking into account $\lambda_{CL_a}$ and $\lambda_{CL_c}$.

As the membrane is not an ideal separation between anode and cathode side, a portion of hydrogen diffuses through the membrane, from anode to cathode side. This hydrogen crossover is considered in the model by meaning of the permeation current (A/cm²) calculation, defined as:

$$i_{crossover} = N_{H_{2MB}} \times 2 \times F \tag{24}$$

where $N_{H_{2MB}}$ is the gas permeation rate of hydrogen through a PFSA membrane, defined by Fick's law and calculated with the dissolved hydrogen concentration gradient across the membrane, defined by Henry's law[82], and the effective diffusion coefficient of hydrogen.

The transport equations at the membrane and catalyst layer interface are coupled with an electrochemical cell voltage law based on a semi-empirical law[83–85]. The cell voltage ($U_{cell}$) is defined as follows:

$$U_{cell} = E_{rev} + \eta + \eta_{ohm} \tag{25}$$

$E_{rev}$ being the reversible voltage:

$$E_{rev} = \frac{\Delta H_0}{2F} + \frac{(\Delta S_0 - \frac{R}{2}\ln(P_{ref}))}{2F}T + \frac{R}{4F}Tln(P_{O_2}) + \frac{R}{2F}T[\ln(P_{H_2}) - \ln(P_{H_2O})] \quad (26)$$

Where $\Delta H_0$ and $\Delta S_0$ are the enthalpy and entropy variation respectively, $R$ is the ideal gas constant, $P_{ref}$ the atmospheric pressure, $T$ the temperature of the membrane, $P_{O_2}$ the partial pressure of $O_2$, $P_{H_2}$ the hydrogen partial pressure, and $P_{H_2O}$ the partial vapor pressure.

The reaction over-potential ($\eta$) is defined as:

$$\eta = \beta_1 + \beta_2 T + \beta_3 Tln(i) + \beta_4 Tln(P_{O_2}) + \beta_5 Tln(P_{H_2O}) + \beta_6 Tln(P_{H_2}) + i\left(\frac{\beta_7}{\sigma_{Clc} \times P_{O_2}} + \frac{\beta_8}{\sigma_{Cla} \times P_{H_2}}\right) \quad (27)$$

And gives the cell voltage as a function of eight $\beta_i$ coefficients, $\sigma_{Clc}$ and $\sigma_{Cla}$, the ionic conductivities of both catalyst layers at the cathode and the anode respectively. The initial $\beta_i$ coefficients values are not provided in this context for reasons of confidentiality.

The internal resistance of a cell $R_T$ includes protonic, electronic and contact resistance noted $R_p$, $R_e$ and $R_c$ respectively. As the electronic resistance is negligible, the ohmic losses ($\eta ohm$) are defined as:

$$\eta ohm = -(Rc + Rp) \times i \quad (28)$$

The contact resistance depends on the materials characteristics. The protonic resistance $Rp$ is defined as:

$$R_p = \frac{e_{MB}}{\sigma_{MB}} \quad (29)$$

where $e_{MB}$ is the thickness of the membrane and $\sigma_{MB}$ is the membrane proton conductivity. The membrane proton conductivity varies with the membrane temperature and the average number of water molecules per sulfonic site of the membrane (λ). It is defined according to Springer's law[18]:

$$\sigma_{MB} = (33.75 \times \lambda - 21.41)e^{\frac{1268}{T}} \quad (30)$$

Subsequent studies with this model will be carried out on a different MEA (MEA 2). To ensure good agreement between simulation results and experimental data, the $\beta_i$ coefficients of the cell voltage law

must be fitted to MEA 2. The methodology and MEA 2 components adopted are described in the following section.

# 3. Calibration of the spatially averaged model: an advanced methodology using a differential cell

The $\beta_i$ coefficients of the semi-empirical over-potential law (Eq. (27)) need to be adjusted to obtain accurate simulation results in a wide range of operating conditions. To identify these parameters, it is necessary to use experimental data from various current densities, gases partial pressure and temperature representative of local conditions in large cell surface area. To achieve greater accuracy, we want to calibrate the model on the local behavior of a PEMFC, i.e. on its local response at different areas (inlet, middle, outlet of the cell). Since these local conditions cannot be measured, and since the experimental or simulation time for a full or partial design of experiment (DOE) with variations in pressure, coolant outlet temperature and relative humidity would be too long, we decided to simulate a few operating conditions at the cell scale in order to recover the local conditions. These simulations are carried out with the model and using the initial $\beta_i$ coefficients from MEA 1 of sub-section 2.1. Once the local conditions have been determined, they are tested with a differential cell, as it is designed to operate as homogeneously as possible and can emulated the local operating of a cell. The methodology is illustrated in Figure 4.

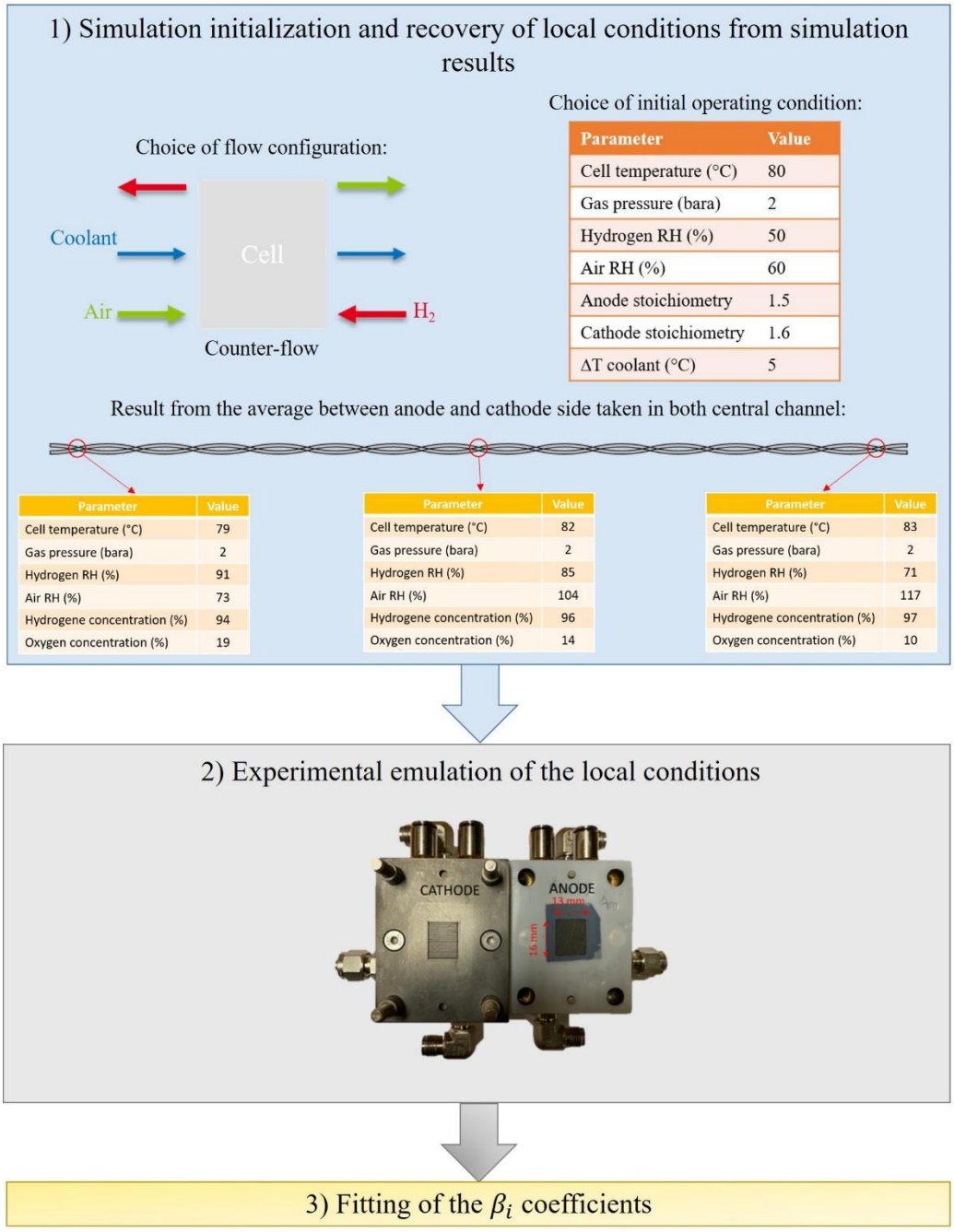


*Figure 4: Illustrated methodology to 1) obtain local conditions for every flow configuration and initial operating condition, to then 2) emulate on a differential cell whose data are used to 3) fit the $\beta_i$ coefficients of the cell voltage law*

The experimental testing protocol is also described in the forthcoming sub-section 3.1.

## 3.1. Differential cell and testing protocol description

A differential or zero gradient PEM fuel cell is usually a small cell designed to ensure as homogeneous in-plane operation as possible, enabling the local conditions of a larger cell to be emulated. The CEA designed cell used in this study has an active surface area of approximatively 2 cm². It presents 32

parallel straight gas channels, machined in graphite plates, with a width of 250 µm and a depth of 400 µm, separated by a rib of 250 µm width (Figure 4 2)).

It is designed to get as little pressure drop as possible between gas inlet and outlet. This, in addition to the rib/channel design and the fact that the cell is used with high flow rates (45 NL/h for the anode and 113 NL/h for the cathode in this study), or very large gas stoichiometry (around 30), allow for uniformity of operation at the inlet/outlet and rib/channel scales. An internal circuit machined into each block regulates the temperature with water. The components chosen for the assembly of MEA 2 include a commercial Catalyst Coated Membrane (CCM) GORE® PRIMEA® MEA, with a 15 µm-reinforced membrane, two electrodes with an anode and cathode Pt loading of 0.1 and 0.4 mg/cm² respectively. A commercial GDL, Sigracet 22BB from SGL Carbon, with a 215 µm thickness in uncompressed state, is used on both sides. As the references of these components are given and due to confidentiality clauses, the authors cannot give detailed values. This assembly is placed in the cell enclosed by a 150 µm thick PTFE hard stop gasket to control the final thickness of the compressed GDL (15-20% of compression).

The cell voltage is controlled by a BioLogic potentiostat (SP-150) coupled with a 20 A booster, combined with EC-Lab control and analysis software. An in-house test bench controls the operating conditions. It allows $H_2$, $O_2$, $N_2$ and air to be used to feed the cell. It is even possible to mix different types of gases and to mix dry and wet gases, with controlled flow rates from 0.5 NL/h to 200 NL/h. This functionality is used in this work to supply the cell with oxygen diluted with nitrogen at various molar fractions. The gases are hydrated by going through temperature-controlled bubblers to reach a targeted relative humidity. Finally, the test bench controls a thermostatic bath that regulates the cell's operating temperature with water.

In this work, the differential cell is used to emulate several operating conditions that can be observed locally on larger cells. To obtain these local operating conditions, three different flow configurations are simulated with the model: counter-flow, with the coolant going in the same direction as the air, co-flow and, finally, counter-flow with the coolant going in the same direction as the hydrogen. For each of the flow configurations, four different operating conditions representative of automotive application operative point, ranging from 60 to 80 °C for the coolant outlet temperature, from 1.1 bara to 2 bara for the gases pressure and a relative humidity of 50/60% for the anode and cathode respectively are simulated thanks to the P3D model[74]. These initially simulated conditions are targeted on a series of experimental tests. This method can be applied to a wider range of RH. Local values of relative humidity, temperature, species concentrations and gas pressure are collected for three different areas of the simulated cell (air inlet, middle and air outlet) at the anode and cathode, giving us 36 local conditions to emulate (methodology illustrated in Figure 4. To these 36 conditions, we add a supplementary operating condition to the experimental protocol. This latter is repeated at the beginning and end of the

test, for short conditioning of the cell and ensure reproducibility. The 37 different operating conditions are referenced in Table 4.

| Cell temperature | Gas pressure anode/cathode | Relative Humidity (RH) anode/cathode | Dry gas concentration $H_2/O_2$ |
|---|---|---|---|
| 80 °C | 2.5/2.3 bara | 95/95 % | 100/21 % |
| 84 °C | 2 bara | 75/61 % | 95/19 % |
| 79 °C | | 75/62 % | 97/19 % |
| 79 °C | | 91/73 % | 94/19 % |
| 82 °C | | 85/104 % | 97/14 % |
| 83 °C | | 82/113 % | 95/9 % |
| 82 °C | | 84/94 % | 96/14 % |
| 80 °C | | 90/107 % | 96/13 % |
| 83 °C | | 71/117 % | 97/10 % |
| 77 °C | | 88/143 % | 97/9 % |
| 78 °C | 1.7 bara | 72/66 % | 98/20 % |
| 82 °C | | 83/63 % | 97/19 % |
| 78 °C | | 100/75 % | 94/19 % |
| 80 °C | | 91/85 % | 98/14 % |
| 83 °C | | 77/112 % | 98/9 % |
| 82 °C | | 91/102 % | 98/14 % |
| 82 °C | | 87/103 % | 96/9 % |
| 79 °C | | 96/105 % | 97/14 % |
| 77 °C | | 95/137 % | 97/9 % |
| 69 °C | 1.5 bara | 77/66 % | 100/20 % |
| 71 °C | | 100/74 % | 100/19 % |
| 70 °C | | 104/113 % | 100/14 % |
| 70 °C | | 104/134 % | 100/14 % |
| 70 °C | | 106/137 % | 100/14 % |
| 69 °C | | 108/79 % | 95/19 % |
| 71 °C | | 102/151 % | 100/9 % |
| 71 °C | | 101/161 % | 100/10 % |
| 69 °C | | 110/177 % | 100/9 % |
| 59 °C | 1.1 bara | 75/68 % | 100/20 % |
| 61 °C | | 99/76 % | 100/19 % |
| 59 °C | | 106/82 % | 96/20 % |

| | | | |
|---|---|---|---|
| 60 °C | | 107/112 % | 100/15 % |
| 60 °C | | 107/137 % | 100/14 % |
| 59 °C | | 109/140 % | 100/14 % |
| 60 °C | | 104/153 % | 100/10 % |
| 63 °C | | 104/170 % | 100/10 % |
| 58 °C | | 114/185 % | 100/10 % |

*Table 4: Operating conditions tested with the differential cell*

Once the desired operating condition is stabilized on the test bench, the potentiostat starts a characterization sequence, which includes a short conditioning period and a current measurement period for a voltage ramp, back and forth. In more detail, the first period is a brief conditioning of the cell. It includes a short period of rest, during which no current can flow and no potential can be applied to the working electrode (i.e. Open Circuit Voltage or OCV), followed by a voltage scan from OCV, to 0.1 V. Finally, a one minute potential step is applied at 0.1 V for performance recovery[86]. The second part of the sequence includes another short period of rest (i.e. OCV) and a measurement of the current during a voltage ramp from 0 V *vs.* OCV to 0.2 V *vs.* Ref and back (i.e. polarization curves measurements) with a scan rate of 1 mV/s. The polarization curves kept to calibrate the electrochemical cell voltage law are those obtained with an increasing voltage ramp.

## 3.2. Fitted parameters

To fit the parameters of Eq. (27), we used a P3D model of the differential cell, including the electrochemical model. Using initial $\beta_i$ coefficients from previous MEA 1 testing, with the input data of the 37 operating conditions and with the physical properties of the components, that model is computed a first time. Using the results from this first simulation, the $\beta_i$ coefficients are adjusted using a linear regression function. Then the model is computed again, with the new set of $\beta_i$ coefficients. These steps are repeated until the ratio of the difference between iteration *n+1* and iteration *n* and the initial value of the $\beta i$ coefficient (first step) is less than $1 \times 10^{-5}$ for each $\beta_i$ coefficients. With a differential cell model, the algorithm is expected to converge quickly, because the current density is uniform. The entire calibration methodology is described in [84].

The $\beta_i$ coefficients values found using this iterative method are listed in Table 5.

| $\beta_1$ | $\beta_2$ | $\beta_3$ | $\beta_4$ | $\beta_5$ | $\beta_6$ | $\beta_7$ | $\beta_8$ |
|---|---|---|---|---|---|---|---|
| -1.0356 V | 0.0020 V/K | -8.345x10$^{-5}$ V/K | 2.42x10$^{-5}$ V/K | 3.0053x10$^{-5}$ V/K | 0 V/K | -1 N/m | 0 N/m |

*Table 5: Fitted value of $\beta_i$ coefficients of the over-potential of the cell voltage law implemented.*

We then compared the simulated and experimental polarization curves (i.e. IV curves), for all the local conditions tested, to assess the quality of the $\beta_i$ coefficients adjustment. The Figure 5 shows the smallest mean relative error between simulated current density and experimental current density for three different cell voltage values (0.6 V, 0.7 V and 0.8 V).

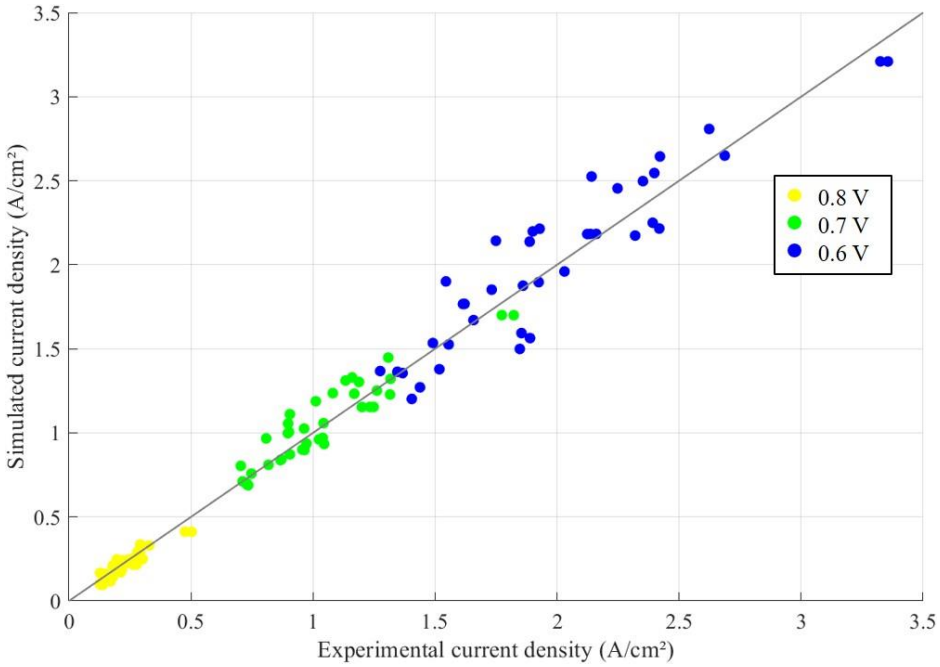


*Figure 5: Simulated vs experimental current density for the 36 local conditions for different cell voltages (0.6 V, 0.7 V and 0.8 V)*

There is a good agreement between the two current densities up to 2 A/cm². In reality, heterogeneity increases with the current density, particularly, at the rib/channel scale, and to a lesser extent, at the inlet/outlet scale. The part of the polarization curves with the highest current density (>2 A/cm²) is the most difficult to fit because it corresponds to the diffusion limit and therefore to the transport of matter. As previously written in section 2.1, the characteristics of the BL and MPL are taken into account in the model to form an effective GDL. Concerning MEA 2, we have information about the BL and MPL forming the GDL Sigracet 22BB from SGL Carbon. We tried to obtain a better fit at the highest current density by slightly adjusting the through-plane tortuosity of the BL and MPL. We ran the $\beta_i$ calibration script, varying the tortuosity values from 1.03 to 1.26 in steps of 0.02 for the BL and from 1.11 to 1.37 in steps of 0.02 for the MPL, always looking at the deviation between the simulated and experimental IV curves. An increase of the deviation was systematically obtained with values different from the initial ones (Table 1). A maximum increase of the deviation from 10.4 % to 11.5 % was noted for the values of BL and MPL tortuosity at 1.26 and 1.36 respectively. The calibration is therefore not very sensitive to variations of BL and MPL tortuosity. Besides, the fit presented in Figure 5 has an $R^2$ of 0.9974, which is a sufficiently high value considering that $R^2$ ranges from 0 to 1. For all the fits tested, the $R^2$ value

ranges from 0.9856 to 0.9974. As the reference current density for the rest of our study does not exceed the value of 2 A/cm² and the R² value for the initial fit is correct, we consider the initial fit sufficient (Figure 5).

# 4. Results and discussion

This section presents the simulation results obtained using the spatially averaged P3D model of the large cell described in section 2. Firstly, a numerical validation of the accuracy of the model is presented in sub-section 4.1, with a comparison of simulation results obtained with the initial P3D model developed in previous studies[74,87] and with the new spatially averaged P3D model. This comparison is realized using the initial set of parameters of MEA 1 (see Table 1) and initial $\beta_i$ coefficients. In the remaining sub-sections, the simulated results are obtained after calibration of the model with the second set of parameters from MEA 2 used for the calibration procedure with the differential cell (sub-section 3.1). All the simulations carried out with the calibrated model are presented in sub-section 4.2. Sub-section 4.3 presents and discusses results from four simulations showing the sensitivity of performance, current and water distribution to coolant operation and relative humidity. Finally, the same set of simulations at high current density is investigated in sub-section 4.4 to show the model predictions abilities.

## 4.1. Comparison of simulations results from the original P3D model and the new spatially averaged P3D model

Two calculations are carried out to validate the spatially averaged approach, using the operating conditions defined in the Table 6 and the parameters in Table 1, in counter-flow configuration, with the coolant flowing in the same direction as the air.

| Comment | Value and units |
|---|---|
| Anode inlet gas pressure | $2x10^5$ Pa |
| Cathode inlet gas pressure | $2x10^5$ Pa |
| Coolant inlet flow rate (fixed) | $9.8x10^{-6}$ $m^3/s$ |
| Anode stoichiometry ratio | 1.5 |

| | |
|---|---|
| Cathode stoichiometry ratio | 1.6 |
| Anode gas inlet temperature | 80 °C |
| Cathode gas inlet temperature | 80 °C |
| Coolant outlet temperature | 80 °C |
| Anode dew point temperature (calculated in relation to the coolant outlet temperature) | 63.5 °C |
| Cathode dew point temperature (calculated in relation to the coolant outlet temperature) | 67.5 °C |
| Fraction of $H_2$ in dry gas | 0.7 |
| Fraction of $O_2$ in dry gas | 0.21 |

*Table 6: Input data implemented in the P3D model and in the spatially averaged P3D model*

Both calculations were performed with 2 x Intel(R) Xeon(R) Gold 6148 CPU at 2.40 GHz. One calculation is carried out with the P3D model (i.e., with detailed flow-field geometry) and the second with the spatially averaged P3D model. Each calculation is performed by increasing the current setpoint to follow a ramp, all physics being resolved at each iteration. In this way, we have the behavior of the cell for a current ranging from 0 to 1.9 A/cm², enabling us to reproduce a polarization curve as measured experimentally. We compare the overall responses of the models with the two IV curves plotted in Figure 6 a). We also compare the average current density calculated along the y-axis (i.e., perpendicular to the flow direction) as a function of the distance between the air inlet and the air outlet of the active surface area, at the specific point of 1.9 A/cm² for both models, as illustrated in Figure 6 b). At each point along the x-axis, we obtain an average value of current called $\overline{\iota_x}$.

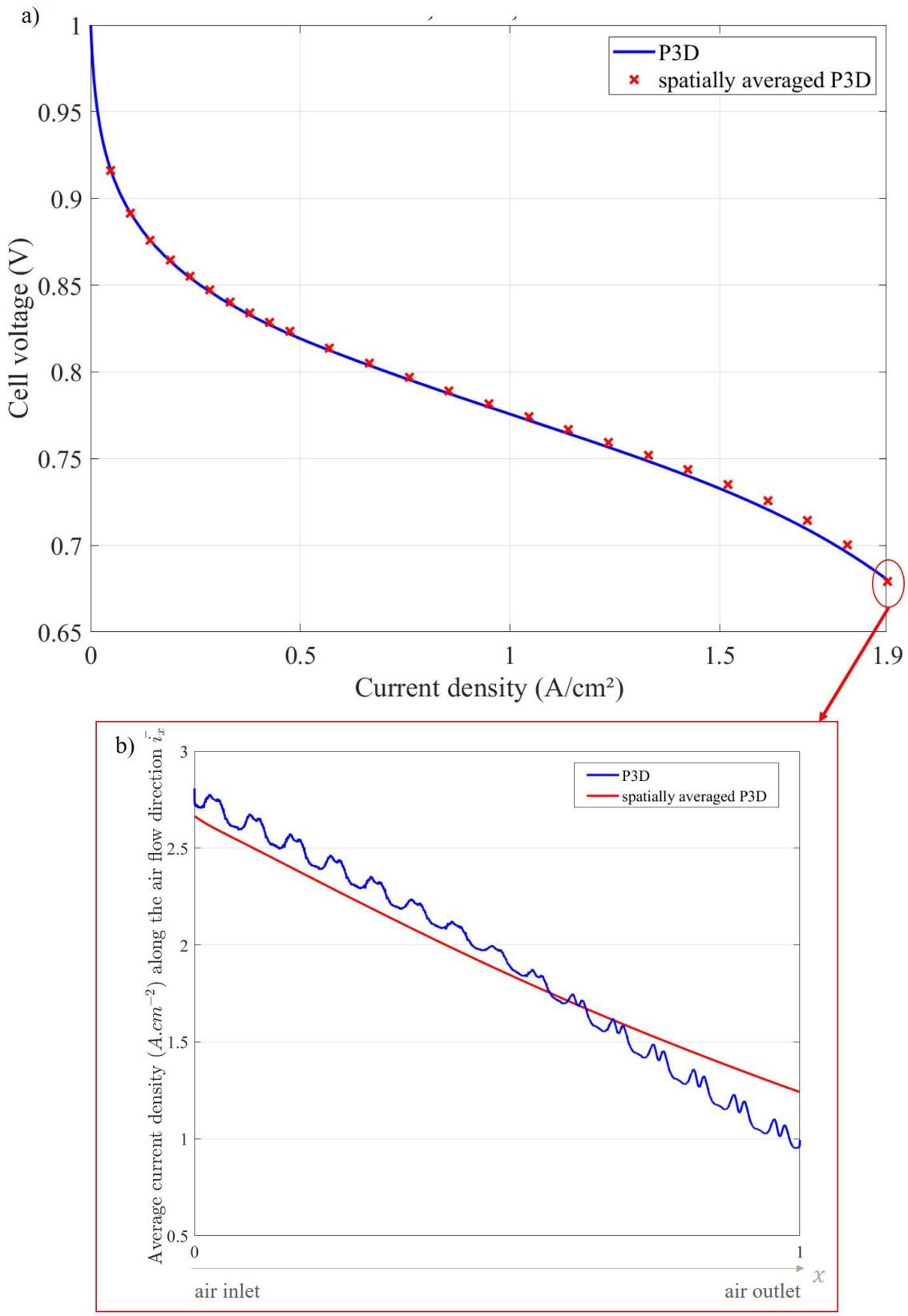


*Figure 6: a) IV curves simulated with the P3D and the spatially averaged P3D model for the 250 cm² PEM fuel cell at 80 °C, 2 bara, 50/60 % RH anode/cathode and 1.5/1.6 stoichiometry anode/cathode, and b) average current density calculated along the y-axis (i.e. perpendicular to the flow direction) simulated with the P3D model and the spatially averaged P3D model at 1.9A/cm².*

The two IV curves overlap almost perfectly up to about 0.79 V (Figure 6 a)). The difference between these two curves then reaches a maximum of 0.05 V at 1.53 A/cm². Figure 6 b) compares the average current density distribution at a specific operating point of 1.9 A/cm². The fluctuations observed on the P3D average current density variations are due to the periodic crossings between the anode and cathode channels. In the spatially averaged model, they do not appear due to the unresolved channels geometry. Apart from these fluctuations, the two average current density curves follow a similar trend and are closely aligned. In fact, the maximum absolute difference between both curves is 0.25 A/cm².

Finally, the Figure 7 shows the current density distribution at 1.9 A/cm² (stationary state) computed with both models, under the same operating condition (80 °C, 2 bara, 50/60 % RH anode/cathode, 1.5/1.6 stoichiometry anode/cathode). Figure 7 is the post-processing taken from a figure provided in the Supplementary Information (Figure S1). The post-processing is necessary to compare both mappings. Indeed, in the initial P3D model distributions, periodic variations of the current density over the active surface are observed due to the alternation of channels and ribs. It is then difficult to directly compare the initial P3D and spatially averaged P3D distributions. To overcome this effect, we divided the active surface into 16*16 small areas and averaged the current density for each area.

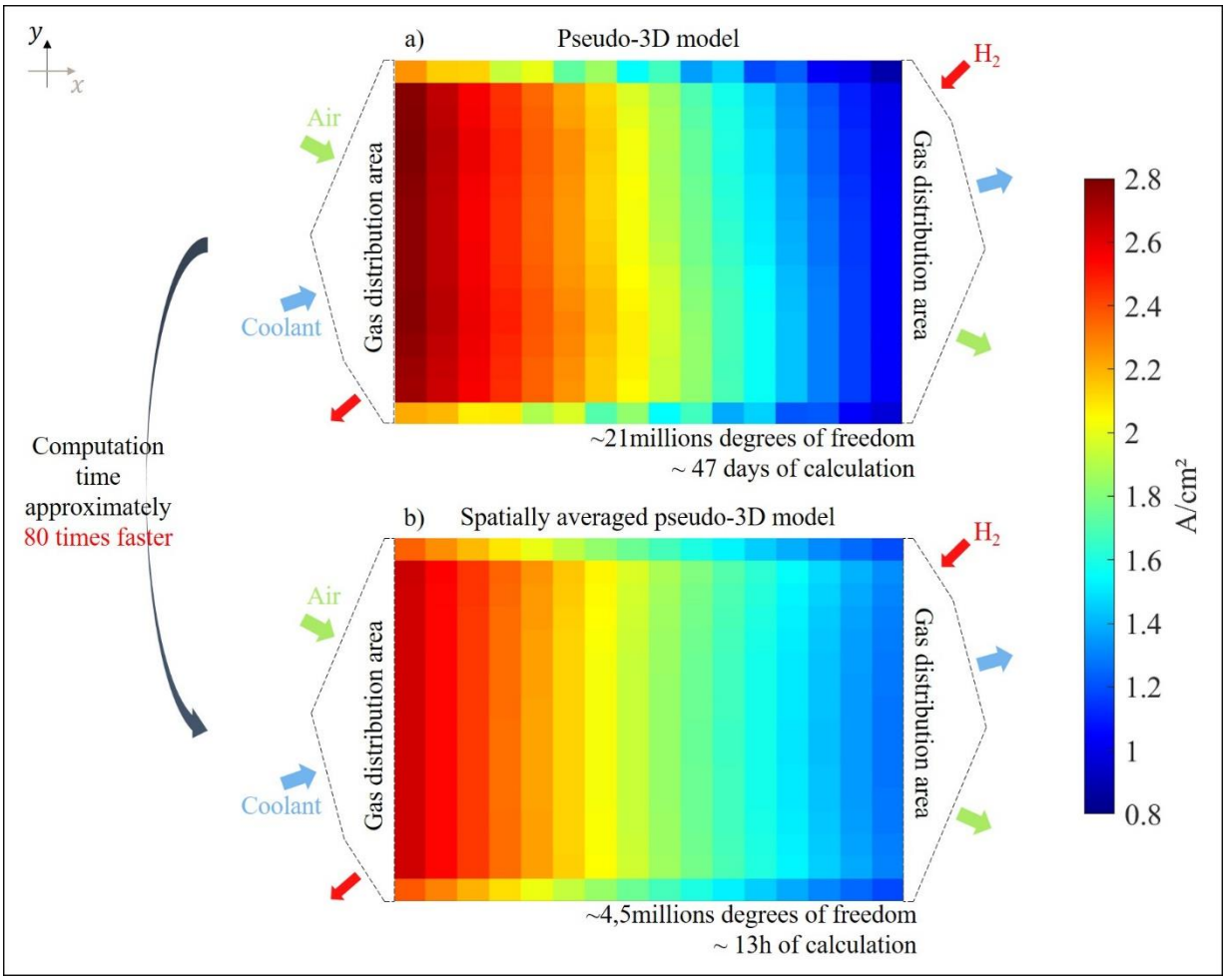


*Figure 7: Distribution of current density simulated with the P3D model on the left and the spatially averaged model on the right for a cell operation at 80 °C, 2 bara, 50/60 % RH anode/cathode, 1.5/1.6 stoichiometry anode/cathode*

The distributions are close together, similar heterogeneities are observed, in the direction of the flow. However, we can observe the small deviation mentioned above, between the two current density distributions. The flow distribution management between the gas distribution areas and the active surface area could explain the small deviation following the y-axis. Indeed, the gas distribution areas are not spatially averaged. In the spatially averaged model, we had to implement a small transition region with isotropic permeability between these two areas, in order to distribute the flow over the entire active surface area and not just in the continuity of the gas distribution channels. It introduces a small approximation that may contribute to the observed differences.

To conclude briefly, the global responses of both models are very close together, regarding both global performance and local heterogeneities. Even if the current density distributions are slightly different, we still observe, with the spatially averaged model, coherent effects and trends that give information about the cell operation. Yet, the computation time of that simulation with the spatially averaged P3D model (13 hours) is divided by a factor of about 80 compared to the computation time of the P3D model for

that specific calculation. This saving in calculation time is very important for the realization of studies like sensitivity analyses of the effect of different operating parameters.

## 4.2. Simulations with the new spatially averaged P3D model

Once validated, the calibrated spatially averaged P3D model allows us to perform a sensitivity analysis of coolant operation and relative humidity. A total of 108 simulations are conducted featuring variations of coolant outlet temperature (60 °C, 70 °C and 80 °C), gas relative humidity (30 %, 50 % and 60 %) and coolant temperature gradient (ΔT) between the inlet and the outlet (2 °C, 6 °C, 10 °C and 20 °C). The cell is supplied with gases in counter-flow configuration, with the coolant flowing in the same direction as the air. The parameters used for the electrochemical model are the one calibrated and detailed in Table 5 and the components characteristics are the one from the components used in the differential cell in sub-section 3.1.

The 108 simulated polarization curves simulated shown in Figure 8 a) highlight the significant impact of these three parameters on cell performances. The Figure 8 b) shows the mean membrane water content over the entire active surface area $\bar{\lambda}$ as a function of current for the 108 simulations.

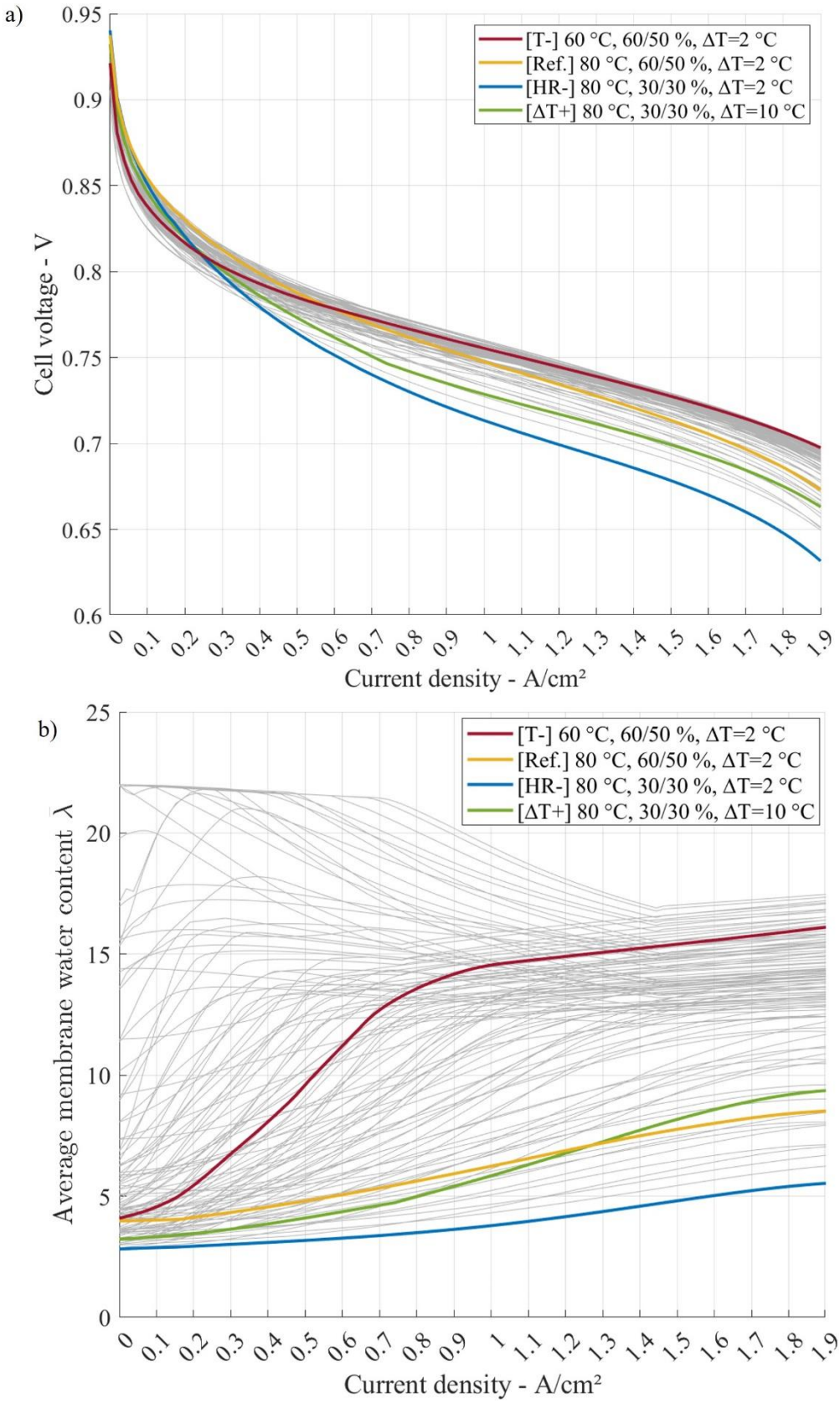


*Figure 8: a) I-V curves and b) water content obtained for the 108 simulations featuring variation in coolant outlet temperature (60 °C, 70 °C and 80 °C), in anode and cathode RH (30 %, 50 % and 60 %) and in ΔT (2 °C, 6 °C, 10 °C) and 20 °C) and performed with the calibrated spatially averaged P3D model. Four curves have been highlighted for later analysis.*

A full investigation of each case is impractical because of the number of operating conditions and the coupled effects between the parameters. Nevertheless, we use the relative standard deviation as a uniformity coefficient (noted $h$ in this study) to quantify the homogeneity of the distribution of the current density i (A/cm²). For its calculation, we divide the standard deviation s of the current density of the entire active surface area (ASA) by the mean current density calculated over the entire active surface area $\bar{\imath}$.

$$h = \frac{s}{\bar{\imath}} \tag{31}$$

$h$ is close to 0 for a distribution with very little deviation from its averaged. This coefficient is calculated for the current density distribution at a current setpoint of 1.9 A/cm², for which the operating heterogeneities are exacerbated. It is plotted for each simulation in Figure 9 as a function of a) coolant outlet temperature, b) coolant temperature gradient, c) gases relative humidity and d) cell voltage to ascertain the impact of these input parameters on the uniformity of current density distribution.

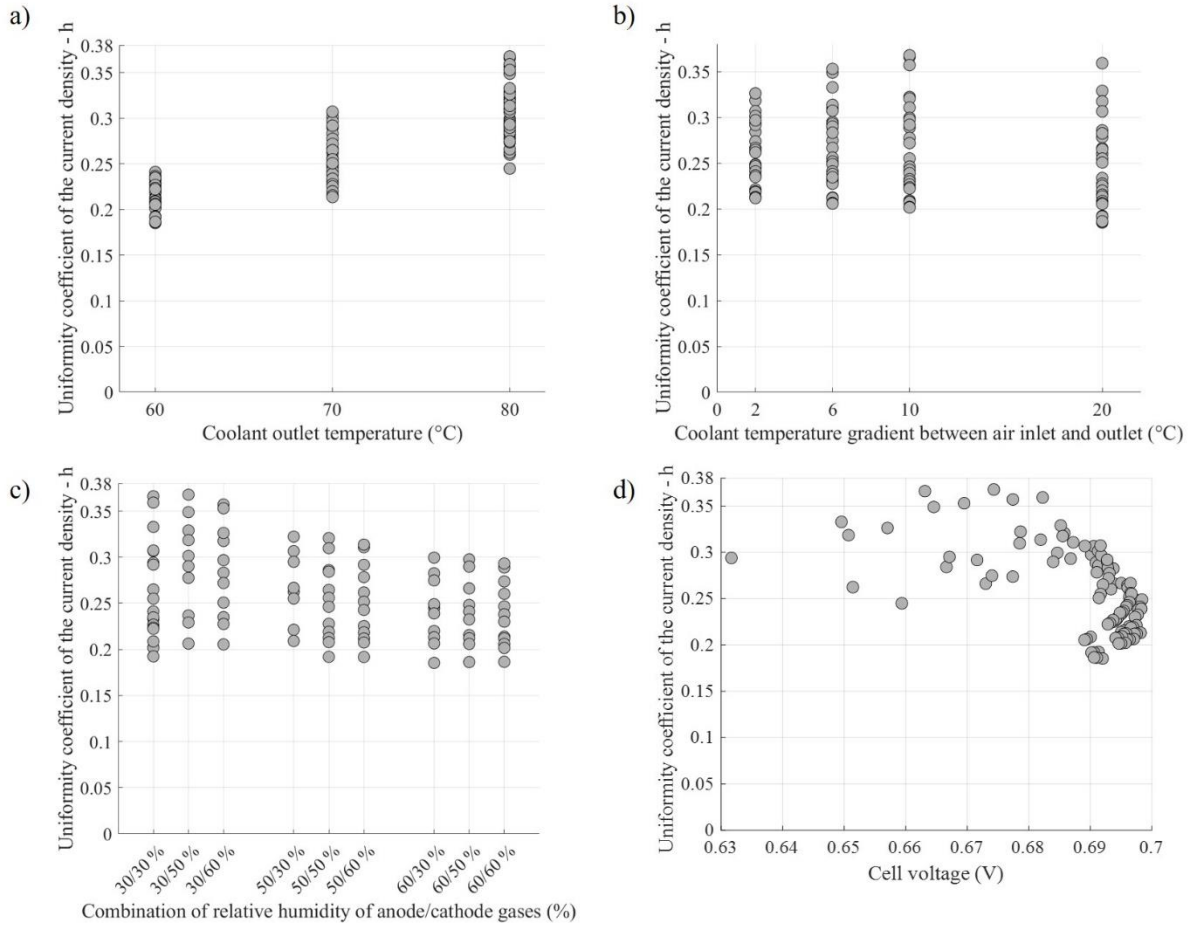


*Figure 9: Coefficient of uniformity h of the current density distribution as a function of a) the coolant outlet temperature (°C), b) the coolant temperature gradient between the air inlet and the outlet (°C), c) the cell voltage (V) and d) the relative humidity of anode/cathode gases (%) for the 108 simulations at a current set point of 1.9 A/cm²*

Figure 9 a) highlights the significant impact of the coolant outlet temperature parameter. Indeed, a lower outlet temperature appears to correlate with a more uniform current distribution. Conversely, an increase in outlet temperature seems to both enhance the heterogeneity of the distribution and expand the range of values for the uniformity coefficients obtained. This suggests that, at higher temperatures, the uniformity of the current distribution is further influenced by other parameters.

The impact of the coolant temperature gradient is shown in Figure 9 b). This latter parameter acts differently on the current density distribution. We can see that as the $\Delta T$ increases, the range of values for the uniformity coefficient extends with lower and higher extreme values. This suggests that at higher temperature gradients, a number of additional parameters, which can either improve or degrade the uniformity of the current density, influences the distribution. However, this trend is less pronounced than that observed for the coolant outlet temperature.

Additionally, Figure 9 c) displays the influence of the anode and cathode relative humidity. If the cathode relative humidity change does not affect the current density distribution, the range of values for the uniformity coefficient seems to narrow around a larger value with increasing relative humidity at the anode. This suggests that higher hydrogen relative humidity results in a more uniform current density distribution. This trend is most apparent when comparing values at 30 % and 60 % at the anode.

Finally, we observe that for simulations with a cell voltage between 0.63 V and 0.69 V at 1.9 A/cm², the uniformity coefficient of the current density distribution varies globally between 0.24 and 0.38. Beyond a voltage of 0.69 V, the coefficient appears to decrease globally, below 0.3 for the majority of the remaining simulations. This suggests that poor cell performances are associated with the most heterogeneous current density distributions. However, the best performances are not obtained with the most uniform current density distributions.

The 108 simulations highlight a different impact of the coolant outlet temperature and coolant temperature gradient on the current density distribution.

Both coolant outlet temperature and coolant temperature gradient appear to have the greatest influence on the uniformity of the current density distribution. Indeed, at higher coolant outlet temperatures and coolant temperature gradient, the range of coefficient values expends, suggesting an increased effect of other parameters. Moreover, the relative humidity acts differently at the anode and at the cathode. If the cathode RH does not affect the current density distribution, a dryer anode RH induces a higher extent as the range of coefficient values expends. Finally, the uniformity of the current density plays an undeniable role in the performance of the cell. Thanks to the model, it is therefore possible to distinguish coupled effects of water coolant operating and relative humidity on the spatial distribution of the current density.

Similar studies can be carried out for the uniformity of the distribution of any other physical quantity over a wide range of operating conditions.

## 4.3. A parametric study with the new spatially averaged model

The detailed results of four operating conditions among the 108 simulations performed with the spatially averaged P3D model are discussed in this sub-section. They correspond to the best and worst as well as medium performances observed in Figure 8 a).The operating conditions for these simulations are also chosen for their diversity of coolant outlet temperature, gas relative humidity and coolant temperature gradient (ΔT) between the cell inlet and outlet, with a view to optimizing the operation and BoP of PEMFC systems. As previously stated in the introduction, an elevated coolant temperature gradient and coolant outlet temperature allow the coolant pump and the humidifiers to be downsized.

We assess the performance of these four operating conditions by means of a basic comparison of IV curves and the durability by means of the temporal variation of the average number of water molecules per sulfonic site of the membrane (λ), a criterion linked to membrane mechanical degradation [88–90]. Indeed, among other things, a variation of the water content in the membrane when the PEMFC undergoes a dynamic load cycle can lead to membrane degradations such as membrane pinholes or cracks [90]. The four sets of operating conditions simulated with the model are described in Table 7.

| **Input data** | **1st operating condition [T-]** | **2nd operating condition [Ref.]** | **3rd operating condition [RH-]** | **4th operating condition [ΔT+]** |
|---|---|---|---|---|
| Anode inlet gas pressure | $2x10^5$ Pa | | | |
| Cathode inlet gas pressure | | | | |
| Initial coolant inlet flow rate of the cell (varies) | $9.788x10^{-6}$ $m^3/s$ | | | |
| Anode stoichiometry ratio | 1.5 | | | |
| Cathode stoichiometry ratio | 1.6 | | | |

| | | | | |
|---|---|---|---|---|
| Fraction of $H_2$ in dry gas | 0.99 | | | |
| Fraction of $O_2$ in dry gas | 0.21 | | | |
| Outlet coolant temperature | 60 °C | 80 °C | 80 °C | 80 °C |
| Coolant temperature gradient between the inlet and the outlet of the cell - ΔT | 2 | 2 | 2 | *10* |
| Anode relative humidity (calculated in relation to the coolant outlet temperature) | 60 % | 60 % | 30 % | 30 % |
| Cathode relative humidity (calculated in relation to the coolant outlet temperature) | 50 % | 50 % | 30 % | 30 % |

*Table 7: Input parameters for the first calculations of the numerical study*

We compare the IV curve response of the model in Figure 8 a) and the average water content over the entire active surface area *vs* the current density in Figure 8 b), for the four operating conditions, named with the abbreviations indicated in Table 7. The second set of operating conditions considered here is the reference condition [Ref.]. The first set [T-] differs by its lower outlet temperature. The other two sets exhibit, at the anode and cathode, a lower relative humidity than the reference, justifying the name [RH-] of the third set, while the fourth one [ΔT+] presents, in addition, a higher temperature gradient.

The impact of temperature on cell behavior can be clearly observed by comparing the IV curves in the [Ref.] and [T-] conditions. Above 0.6 A/cm², the simulation in conditions [T-] shows a higher cell voltage (red curve). On the contrary, at lower current density, the performance is reduced in conditions [T-], due to a lower activation at 60 °C. Indeed, the positive effect of the temperature decrease is offset below 0.6 A/cm² by a negative effect, namely a loss of catalytic activity.

The impact of relative humidity on cell behavior is observed by comparing the IV curves [Ref.] (yellow curve) and [RH-] (blue curve). It is clear that drier conditions are associated with poorer performance. This difference in performance can be seen even at low current density on the IV curves (above 0.1 A/cm² in this case).

Focusing on dry conditions, the comparison of the IV curves of conditions [RH-] and [ΔT+] demonstrates that the temperature gradient of the coolant plays an important role. Below 0.3 A/cm², performances are quite similar as they mainly depend on the activation over-potential. Above 0.3 A/cm², a bigger temperature gradient between the inlet and outlet ($\Delta T = 10\ °C$) induces a higher cell voltage. It has to be noted that the global relative humidity of a cell is calculated using the outlet temperature of the coolant, equivalent to the air outlet. As the air at the cell inlet is cooler when the coolant $\Delta T$ is higher, it induces a better hydration of the membrane at the cathode inlet, allowing a higher membrane water content distribution along the air channel, fostered by water production. However, starting from the [RH-] conditions, it appears that either an increase in relative humidity or a decrease in temperature gradient can be beneficial to cell performance. Comparing the IV curves of [Ref.] (yellow curve) and [ΔT+] (green curve), we observe that, above 0.1 A/cm², cell voltage is higher when increasing relative humidity rather than temperature gradient. The gap between these two curves is widening until 0.8 A/cm² (gap of 0.02 V) and then narrows, reaching a gap of 0.01 V at the end of the curve (1.9 A/cm²).

With the intention to better understand the influence of the temperature, the relative humidity and the coolant temperature gradient on the cell performance, Figure 8 b) displays the variation of the mean water content of the membrane over the entire active surface area with the current density.

The highest water content and highest variation in water content occurs for [T-], operating condition for which the best performance is obtained. The higher performance for [T-] could therefore be attributed to a better humidification of the membrane at 60 °C. Indeed, the lower coolant outlet temperature allows increasing the membrane water content and thereby enhances its conductivity. However, it should be noted that the relative humidity of the gases in the channels rises rapidly under this condition and quickly exceeds 100 %. In fact, with a single-phase model, flooding phenomena are not taken into account, so the performance of a cell in the event of heavy humidification, which is promoted at 60 °C, may be overestimated.

On the contrary, for [RH-], the water content and its variation with current density are significantly lower than for other conditions. [RH-] is both the driest condition and the poorest in performance. Comparing [RH-] and [ΔT+], we observe that increasing the temperature gradient from 2 °C to 10 °C allows a bigger increase in water content when the current density rises, even if both curves start from almost the same water content at low current density. From those comparisons, better humidification implies better overall performance.

As far as [Ref.] and [ΔT+] are concerned, this latter trend is confirmed up to 1.2 A/cm². Indeed, we observe a higher water content for [Ref.], corresponding to a better performance up to that point. However, the water content variation is more important for [ΔT+] and, above 1.2A/cm², the trend in water content reverses. We then observe higher water content for an operating condition that gives

poorer performance, which is contradictory with previous trends. A closer look at the distribution of water content (Figure 8 a)) indicates that it is from this point (1.2 A/cm²) onwards that the gap between the two IV curves narrows. We can assume that both the water production before 1.2 A/cm² and the higher temperature gradient are not sufficient to counterbalance the overall dryness of the cell in [ΔT+] conditions. Nevertheless, the temperature gradient still permits a recovery of performance loss due to a lack of humidification, if the current density is above a certain threshold. This allows for a de facto catch-up in performance relative to that achieved with higher relative humidity.

## 4.4. Analysis of spatial heterogeneities

We study the current density and water content distribution at high current density (1.9 A/cm²) for the four operating conditions presented previously ([Ref.], [ΔT+], [T-] and [RH-]). As an example, we first focus on the [ΔT+] case. It allows to illustrates the in-plane distributions that can be generated by the spatially average P3D model for each layer implemented (Membrane, CL, GDL, GC, CWC and BP). Figure 10 depicts the distributions of a) cathode-side metal plate temperature, b) current density, c) relative humidity in the cathode gas channels and d) membrane water content obtained for this simulation.

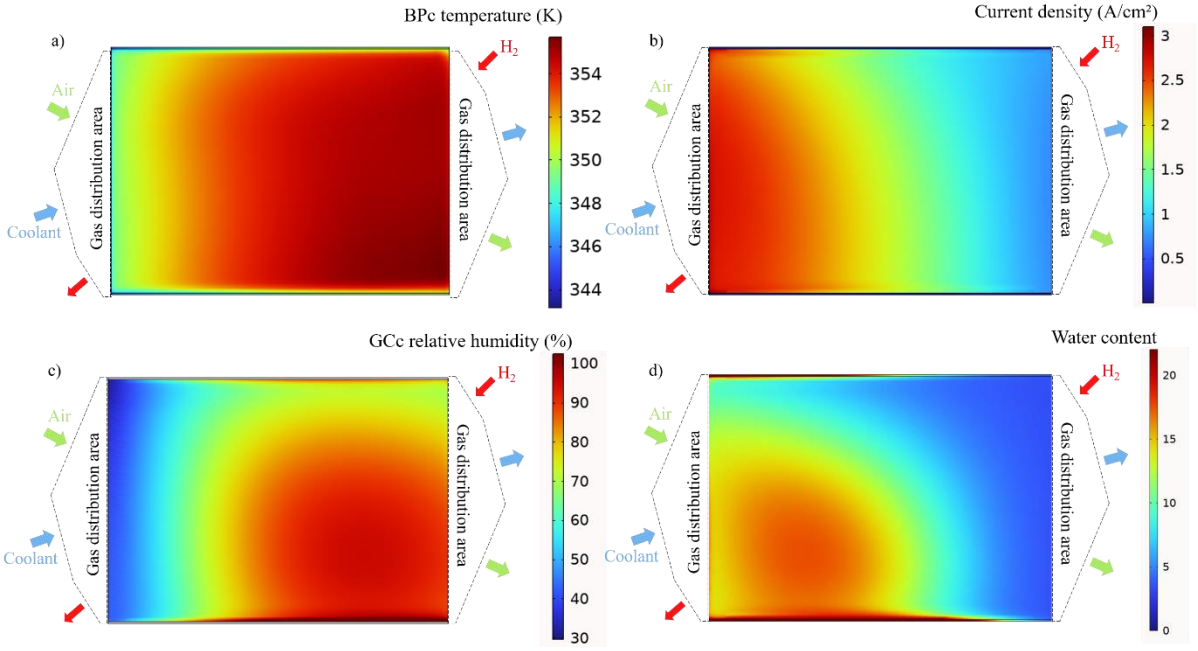


*Figure 10: a) BPc temperature, b) current density, c) GCc relative humidity and d) water content distributions after simulation of [ΔT+] case*

As the cell geometry consists of parallel-wavy channels for the anode fluid and for the cathode fluid, and the resulting cooling circuit in the x-direction, stronger parameter gradient appears along the channel length. Moreover, temperature, current density variation and relative humidity heterogeneities are also observed in the y-directions due to the non-uniform water-cooling and gas velocity distribution at the

inlet. Indeed, Figure 11 shows the heterogeneities in the fluid velocities along a line situated on the y-axis at the air inlet, middle and air outlet of the active surface area.

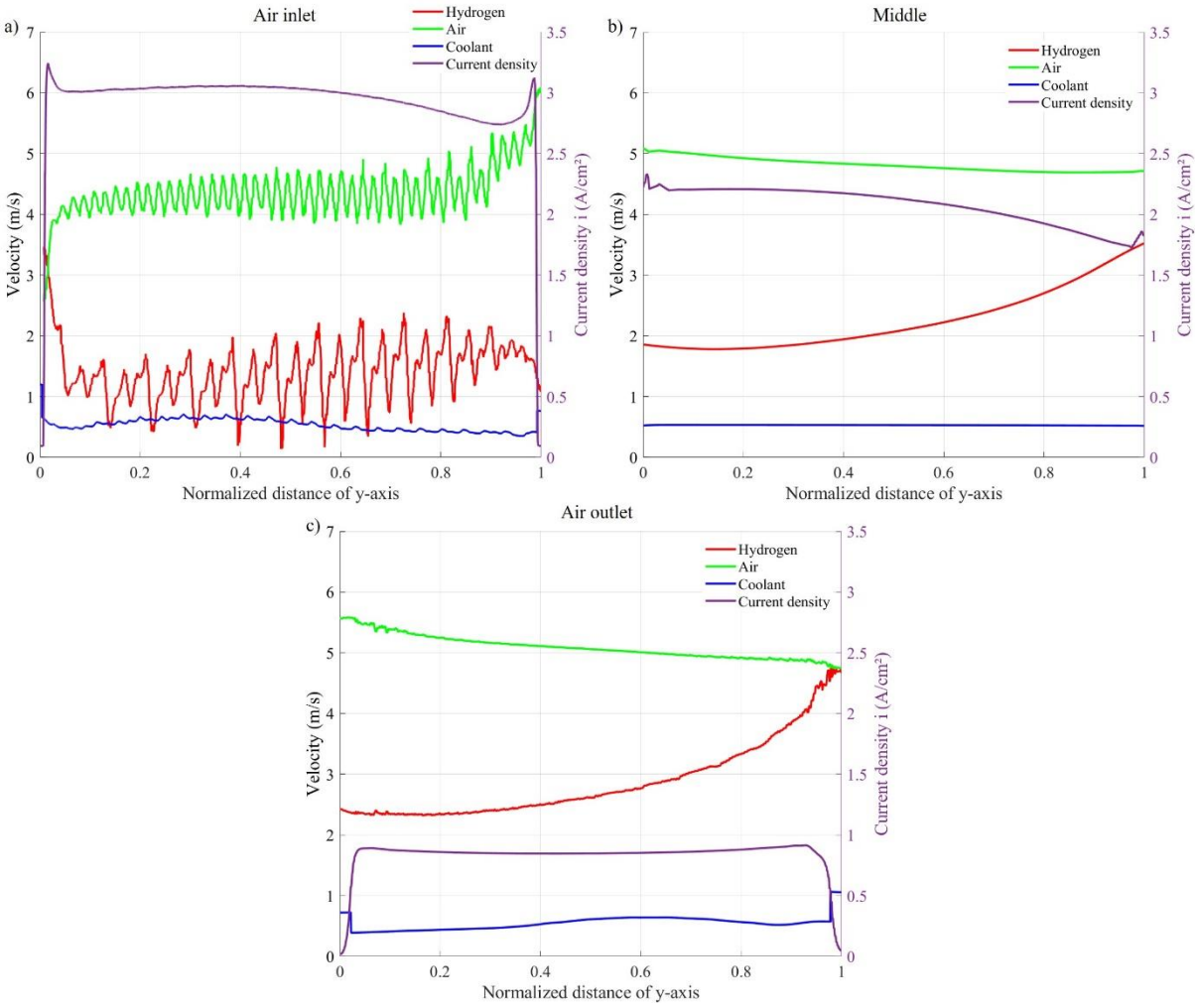


*Figure 11: Gas and coolant velocity in their respective channels on a line along the y-axis located at a) the cell air inlet, b) the middle of the cell and c) the cell air outlet*

The heterogeneities observed along x-axis are due the reactant gas consumption and water-cooling temperature change. The ones observed along the y-axis on either side of the active surface are primarily a consequence of the configuration of the fluid distribution areas. Despite the spatial averaging of exchanged fluxes, channels permeability and GDL tortuosity, the model still captures heterogeneities not only on the x-axis, but also on the y-axis. This proves the necessity to keep a model considering variations along the y-axis, able to predict specific mappings for each layer implemented (Membrane, CL, GDL, GC, CWC and BP).

For sake of clarity, the average current density and water content of the membrane, calculated along the y-axis (i.e. perpendicular to the flow direction), respectively noted $\bar{\iota}_x$ and $\bar{\lambda}_x$, are plotted in the Figure 12 for the four operating conditions at 1.9 A/cm².

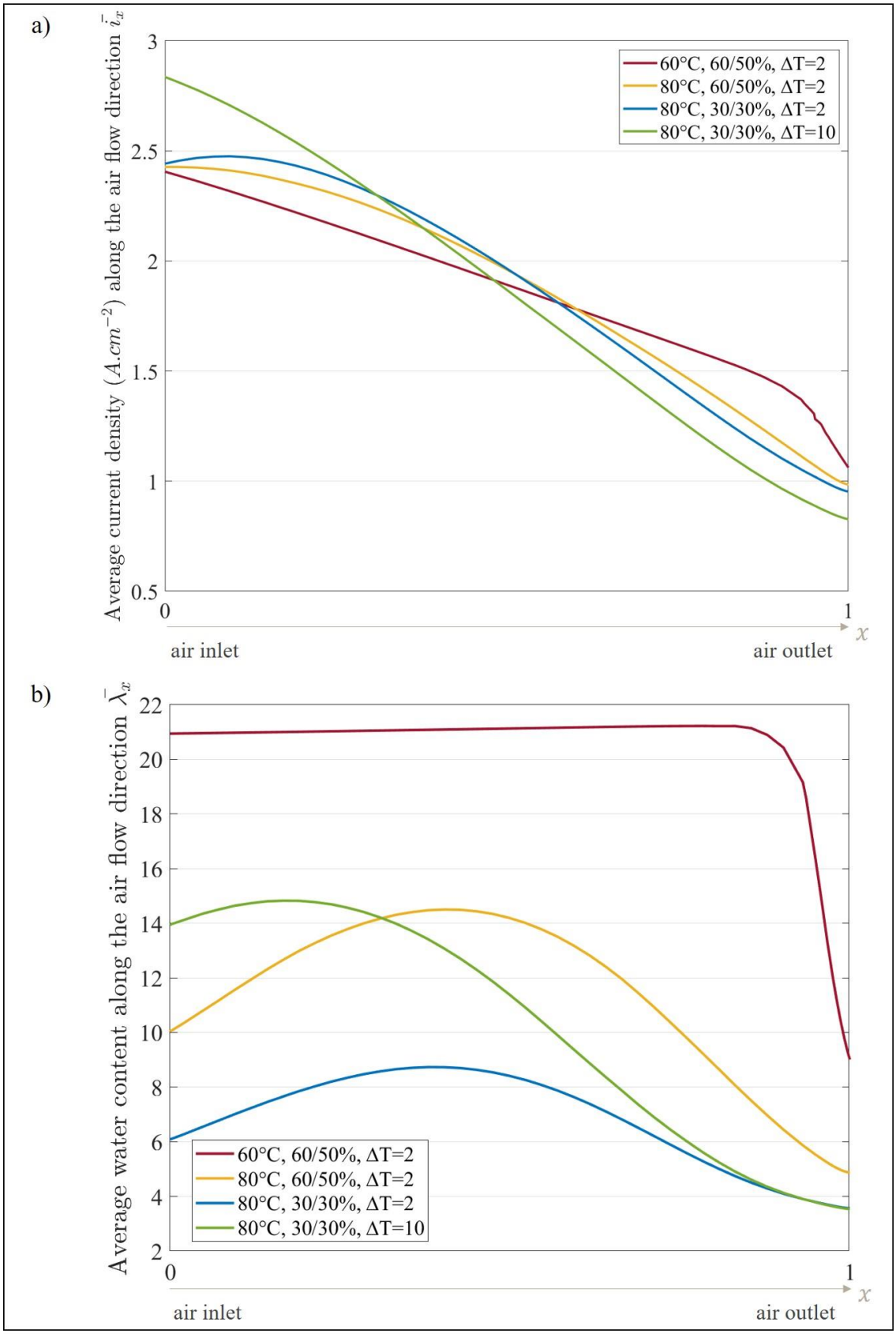


*Figure 12: Average of the (a) current density and (b) membrane water content values at 1.9 A/cm² calculated by line perpendicular to the direction of flow for four operating conditions: [Ref.] – 80 °C, 60/50 %, ΔT=2 °C, [T-] – 60 °C, 60/50 %, ΔT=2 °C, [RH-] – 80 °C, 30/30 %, ΔT=2 °C et [ΔT+] – 80 °C, 30/30 %, ΔT=10 °C*

By comparing the conditions [Ref.] and [RH-] in Figure 12, we can confirm the trend that better membrane humidification means better performance. In fact, the two curves have a similar current density distribution (Figure 12 a)) and similar water content distribution (Figure 12 b)) at 1.9 A/cm², but the water content is simply higher for conditions [Ref.], which exhibits the best performance (see figure 8 a). As both water content distributions are very similar in their shape, we can say that the distribution is characteristic of a temperature gradient of 2 °C between the inlet and the outlet at 80 °C and 1.9 A/cm².

We observe a significantly greater amount of water present along the flow direction (Figure 12 b)) under the wettest condition [T-]. In fact, the water content curve shows a steady plateau up to the hydrogen inlet, where the water content decreases following the air flow (from left to right). As the water content almost reach 22, we assume that the membrane is in contact with liquid water, as explained in sub-section 2.3. Because of this limit, we certainly cannot see the humidification trend curve at the air inlet that we observe for the other conditions. Therefore, it is not easy to see the influence of the temperature gradient on the water distribution for this operating condition. However, it was observed in a previous study[87] that the water content profile in the membrane depends mainly on the relative humidity profile of the gases at the anode. This can be explained by the fact that flux exchanges in pure hydrogen take place more rapidly than at the cathode. In fact, the large quantity of water visible at the air inlet is due to the fact that the hydrogen has accumulated water up to its outlet and the smaller amount at the air outlet is the inflow of dry hydrogen. In addition, we can see in Figure 12 a) that the current density decreases, mostly following the depletion of oxygen, and shows a drop following the water content at the air outlet. It suggests that the distribution of the water in the membrane along the flow direction has an impact on the distribution of the current density.

Even though the condition [ΔT+] exhibits a water content curve comparable in shape to the condition [Ref.] (Figure 8 b)), it shows a distribution of water content quite different from the other curves at 80 °C (Figure 12 b)). For a higher temperature gradient [ΔT+], the peak of the curve shifts towards the cell entrance but with almost the same amplitude as for the condition [Ref.]. This confirms the hypothesis that the membrane is better hydrated at the cathode inlet in this case. However, the high temperature gradient impedes the uniformity of the distribution of the water content or of the current density (Figure 12 a)). Nevertheless, the amount of water obtained at the cell inlet corresponds almost perfectly to the amount of water in the middle of the cell for the wetter condition [Ref.] at such a high current density (1.9 A/cm²). Therefore, even if cell operation at 80 °C, 30/30 % RH and ΔT=10 °C exhibits the most heterogeneous current density distribution along the air channel, the temperature gradient fosters the membrane water content in order to maintain quite good performance in drier operating condition. It is noteworthy that the condition [RH-] exhibits a more homogeneous current density distribution, with a lower performance corresponding to a more homogeneous yet lower water content. As with the observations at different current densities, it would be possible to use the model to

anticipate local degradations of the membrane in relation to strong variations in membrane water content along the flow, for a given operating point. Indeed, local drying, as observed at the air outlet for [T-], could be the site of membrane degradation.

In essence, these plots show that the model captures well the heterogeneities of the current density and membrane water content distributions between the inlet and outlet of the cell, and that the simulation results show expected and consistent trends for the chosen operating conditions. These graphs also show the influence of the temperature gradient and gas relative humidity on the membrane water content distribution. It may therefore be possible to manage the distribution of the membrane's water content and its amplitude by managing the RH and the coolant temperature gradient. At this stage, the information provided by these curves is still not sufficient to establish a clear link between uniformity of current density or water content and cell performance.

## 5. Conclusion

The study of the influence of spatial variations of operating parameters over the whole active area of large fuel cells is now eased by the development of a spatially averaging method added to a P3D modelling approach developed previously[74]. It provides insight into the current density, temperature, species concentrations and relative humidity distribution, from cell inlet to outlet and over the entire MEA area and takes into account coolant physics, which is not common in PEMFC modelling. For sake of accuracy, a well-adjusted electrochemical cell voltage law taking into account local operation conditions is of paramount of importance. To do so, a methodology for adjusting the electrochemical parameters of the semi-empirical law is implemented in the model from experimental measurements on a differential cell emulating the local condition on a large cell surface area. The spatially averaged P3D model was successfully validated against the previous P3D model and was used to simulate more than a hundred operating conditions.

These results have shown the influence of coolant outlet temperature and temperature gradient and relative humidity on the distribution of current density and water content along the air flow, but also on the performance of the cell and the evolution of its water content as a function of current density. We have introduced a coefficient of variation that evaluates the uniformity of physical parameters over the active area. The best performance does not correlate with the most uniform current density distribution. However, the water content in the membrane has a significant influence on the performance and can be controlled both by the humidity of the gases, as is traditionally done, and by the coolant operation. By increasing the temperature gradient in dry conditions (i.e. reducing the cell inlet temperature), we can manage to improve the hydration of the membrane at the air inlet and tend toward the performances that we would have in much more humid conditions with a smaller gradient. Moreover, increasing the temperature gradient could result in a downsizing of the coolant pump of the fuel cell system, while

increasing the relative humidity means that the air humidification device would need to be oversized. In a general context where increasing the temperature of the stack is targeted by many fuel cell developers, the balance between air humidification and stack temperature gradient could become a crucial aspect towards the optimization of the system.

In conclusion, the spatially averaged P3D model is a useful tool for studying operational heterogeneities at the cell scale, predicting stack performance and durability, and optimizing management by selecting the most appropriate operating conditions through system control. It should be noted that this approach does not capture the variation of local parameters induced by the rib to channel geometry only accessible with a full 3D channel/rib model representing only ~1/1000 of a large cell surface area. However, the spatially averaged P3D model provides a better understanding and insight of the influence of the coolant outlet temperature and temperature gradient on the functioning of the cell thanks to simulations that are easier to realize than experimental studies. Moreover, the computation time for this model is up to 80 times shorter than the previous P3D model and is shorter than any model with this level of prediction encountered in the literature by the authors.

As a perspective, further studies should be carried out and combine the results of the model with experimental studies on durability to investigate the link between the membrane water content and membrane degradations. The degradation phenomena of PEM cell are complex, but the possibilities offered by the model could enable us to go further in understanding these phenomena and even develop strategies for anticipating membrane degradation.

## References


1. U.S. Department of Energy, *energy.gov* (2016) https://www.energy.gov/eere/fuelcells/articles/comparison-fuel-cell-technologies-fact-sheet.

2. European Hydrogen Observatory, *Obs.-Hydrog.* https://observatory.clean-hydrogen.europa.eu/learn-about-hydrogen/hydrogen-basics/hydrogen-value-chains.

3. R. Can Samsun and M. Rex, *Deployment of Fuel Cell Vehicles in Road Transport and the Expansion of the Hydrogen Refueling Station Network: 2023 Update*, (2023) https://www.ieafuelcell.com/fileadmin/publications/2023/2023_Deployment_of_Fuel_Cell_Vehicles_and_Hydrogen_Refueling_Station.pdf.

4. D. D. Papageorgopoulos, *Renew. ENERGY*.

5. T. Miao et al., *Energy*, **239**, 121922 (2022).

6. D. J. L. Brett et al., *J. Power Sources*, **172**, 2–13 (2007).

7. B. Feng, R. Lin, D. Liu, and D. Zhong, *Int. J. Electrochem. Sci.*, **14**, 2175–2186 (2019).

8. G. Maranzana, O. Lottin, T. Colinart, S. Chupin, and S. Didierjean, *J. Power Sources*, **180**, 748–754 (2008).

9. A. M. Abdullah, T. Okajima, A. M. Mohammad, F. Kitamura, and T. Ohsaka, *J. Power Sources*, **172**, 209–214 (2007).

10. I. Alaefour, G. Karimi, K. Jiao, and X. Li, *Appl. Energy*, **93**, 80–89 (2012).

11. S. Basu, M. W. Renfro, and B. M. Cetegen, *J. Power Sources*, **162**, 286–293 (2006).

12. S. Rodosik, thesis, Université Grenoble Alpes (2019) https://theses.hal.science/tel-02493175.

13. Q. Li, R. He, J.-A. Gao, J. O. Jensen, and N. J. Bjerrum, *J. Electrochem. Soc.*, **150**, A1599–A1605 (2003).

14. Y. Si, R. Jiang, J.-C. Lin, H. R. Kunz, and J. M. Fenton, *J. Electrochem. Soc.*, **151**, A1820–A1824 (2004).

15. F. Barbir, in *PEM Fuel Cells*, F. Barbir, Editor, p. 17–32, Academic Press, Burlington (2005) https://www.sciencedirect.com/science/article/pii/B9780120781423500033.

16. F. Barbir, in *PEM Fuel Cells*, F. Barbir, Editor, p. 33–72, Academic Press, Burlington (2005) https://www.sciencedirect.com/science/article/pii/B9780120781423500045.

17. D. M. Bernardi and M. W. Verbrugge, *J. Electrochem. Soc.*, **139**, 2477–2491 (1992).

18. T. E. Springer, T. A. Zawodzinski, and S. Gottesfeld, *J. Electrochem. Soc.*, **138**, 2334 (1991).

19. J. Marcinkoski,.

20. B. James,.

21. B. D. James and S. A. Inc,.

22. D. Curtin, R. Lousenberg, T. Henry, P. Tangeman, and M. Tisack, *J. Power Sources*, **131**, 41–48 (2004).

23. T. F. Fuller and J. Newman, *J. Electrochem. Soc.*, **140**, 1218 (1993).

24. P. Houchang et al., *J. Power Sources*, **227**, 72–79 (2013).

25. *CoLab* https://colab.ws/articles/10.1016%2Fj.jpowsour.2008.01.020.

26. C.-Y. Lee, S.-J. Lee, Y.-M. Lo, and Y.-M. Liu, *Int. J. Electrochem. Sci.*, **9**, 272–281 (2014).

27. S. Basu, M. Renfro, H. Gorgun, and B. Cetegen, *J. Power Sources*, **159**, 987–994 (2006).

28. S. Dutta and S. Shimpalee, *Numer. Heat Transf. Part -Appl. - NUMER HEAT Transf. PT -APPL*, **38**, 111–128 (2000).

29. M. Wang, H. Guo, and C. Ma, *J. Power Sources*, **157**, 181–187 (2006).

30. Z. Liu, Z. Mao, C. Wang, W. Zhuge, and Y. Zhang, *J. Power Sources*, **160**, 1111–1121 (2006).

31. Q. Yan, H. Toghiani, and H. Causey, *J. Power Sources*, **161**, 492–502 (2006).

32. C. Bao, M. Ouyang, and B. Yi, *Int. J. Hydrog. Energy*, **31**, 1040–1057 (2006).

33. Y. Huang et al., *Energy Convers. Manag.*, **254**, 115221 (2022).

34. J. Choi, Y.-H. Kim, Y. Lee, K.-J. Lee, and Y. Kim, *J. Mech. Sci. Technol.*, **22**, 1417–1425 (2008).

35. E. Afshari, M. Ziaei-Rad, and Z. Shariati, *Int. J. Hydrog. Energy*, **41**, 1902–1912 (2016).

36. Y. Vazifeshenas, K. Sedighi, and M. Shakeri, *Appl. Therm. Eng.*, **147**, 81–89 (2019).

37. S. Li and B. Ake Sunden, *Int. J. Numer. Methods Heat Fluid Flow*, **28**, 1684–1697 (2018).

38. S. H. Yu, S. Sohn, J. H. Nam, and C.-J. Kim, *J. Power Sources*, **194**, 697–703 (2009).

39. S. M. Baek, S. H. Yu, J. H. Nam, and C.-J. Kim, *Appl. Therm. Eng.*, **31**, 1427–1434 (2011).

40. Y. Kai, Y. Kitayama, M. Omiya, T. Uchiyama, and M. Kato, *J. Fuel Cell Sci. Technol.*, **10** (2013).

41. Z. Zhang, J. Mao, and Z. Liu, *Int. Commun. Heat Mass Transf.*, **153**, 107376 (2024).

42. X. Liu et al., *Int. J. Hydrog. Energy*, **48**, 23681–23705 (2023).

43. L. C. Pérez, L. Brandão, J. M. Sousa, and A. Mendes, *Renew. Sustain. Energy Rev.*, **15**, 169–185 (2011).

44. D. S. Hussey, D. L. Jacobson, M. Arif, K. J. Coakley, and D. F. Vecchia, *J. Fuel Cell Sci. Technol.*, **7**, 021024 (2010).

45. T. Trabold et al., in *Handbook of Fuel Cells*, (2010).

46. R. Alink and D. Gerteisen, *Int. J. Hydrog. Energy*, **39**, 8457–8473 (2014).

47. Garcıa-Salaberri, D. Sanchez, P. Boillat, M. Vera, and K. A. Friedrich, *J. Power Sources*, **359**, 634–655 (2017).

48. L. Pant et al., *Electrochimica Acta*, **326**, 134963 (2019).

49. Y. Wang and C.-Y. Wang, *Electrochimica Acta*, **50**, 1307–1315 (2005).

50. Y. Wang and C.-Y. Wang, *Electrochimica Acta*, **51**, 3924–3933 (2006).

51. H. Wu, P. Berg, and X. Li, *J. Electrochem. Soc.*, **157**, B1 (2009).

52. S. Culubret, M. A. Rubio, D. G. Sanchez, and A. Urquia, *Int. J. Hydrog. Energy*, **45**, 5710–5722 (2020).

53. Z. Zhang, L. Jia, X. Wang, and L. Ba, *Int. J. Energy Res.*, **35**, 376–388 (2011).

54. Y. Wang, S. Basu, and C.-Y. Wang, *J. Power Sources*, **179**, 603–617 (2008).

55. G. Zhang and K. Jiao, *J. Power Sources*, **391**, 120–133 (2018).

56. C.-Y. Wang, M. Groll, S. Rösler, and C.-J. Tu, *Heat Recovery Syst. CHP*, **14**, 377–389 (1994).

57. R. B. Ferreira, D. S. Falcão, V. B. Oliveira, and A. M. F. R. Pinto, *Appl. Energy*, **203**, 474–495 (2017).

58. G. Zhang, L. Fan, J. Sun, and K. Jiao, *Int. J. Heat Mass Transf.*, **115**, 714–724 (2017).

59. M. Secanell et al., *ECS Trans.*, **64**, 655–680 (2014).

60. *COMSOL* https://www.comsol.com/release/5.6/fuel-cell-and-electrolyzer-module.

61. https://www.ansys.com/products/fluids/ansys-fluent.

62. D. Cheddie and N. Munroe, *J. Power Sources*, **147**, 72–84 (2005).

63. C. Siegel, *Energy*, **33**, 1331–1352 (2008).

64. M. Arif, S. C. P. Cheung, and J. Andrews, *Energy Fuels*, **34**, 11897–11915 (2020).

65. J. Zhao, X. Li, C. Shum, and J. McPhee, *Energy AI*, **6**, 100114 (2021).

66. O. B. Rizvandi and S. Yesilyurt, *Electrochimica Acta*, **324**, 134866 (2019).

67. G. Zhang, J. Wu, Y. Wang, Y. Yin, and K. Jiao, *Int. J. Heat Mass Transf.*, **150**, 119294 (2020).

68. C. M. Baca, R. Travis, and M. Bang, *J. Power Sources*, **178**, 269–281 (2008).

69. C. Yin et al., *Appl. Energy*, **348**, 121543 (2023).

70. Y. Zou et al., *Energies*, **16**, 5932 (2023).

71. E. Rahmani, T. Moradi, S. Ghandehariun, G. F. Naterer, and A. Ranjbar, *Energy*, **264**, 126115 (2023).

72. H. Liu et al., *Appl. Therm. Eng.*, **174**, 115313 (2020).

73. B. Chen et al., *Energy*, **285**, 128933 (2023).

74. F. Nandjou, J.-P. Poirot-Crouvezier, M. Chandesris, and Y. Bultel, *Int. J. Hydrog. Energy*, **41**, 15545–15561 (2016).

75. F. Nandjou, thesis, Université Grenoble Alpes (2015) https://theses.hal.science/tel-01267255.

76. E. Tardy, thesis, Université Grenoble Alpes (2021) https://www.theses.fr/2021GRALI103.

77. J.-D. Chen, *J. Colloid Interface Sci.*, **109**, 341–349 (1986).

78. H. Wong, S. Morris, and C. J. Radke, *J. Colloid Interface Sci.*, **148**, 317–336 (1992).

79. K.-K. Tio, C. Y. Liu, and K. C. Toh, *Heat Mass Transf.*, **36**, 21–28 (2000).

80. F. Meier and G. Eigenberger, *Electrochimica Acta*, **49**, 1731–1742 (2004).

81. T. A. Zawodzinski, J. Davey, J. Valerio, and S. Gottesfeld, *Electrochimica Acta*, **40**, 297–302 (1995).

82. W. Henry and J. Banks, *Philos. Trans. R. Soc. Lond.*, **93**, 29–274 (1997).

83. J. C. Amphlett, R. F. Mann, B. A. Peppley, P. R. Roberge, and A. Rodrigues, *J. Power Sources*, **61**, 183–188 (1996).

84. P. Schott and P. Baurens, *J. Power Sources*, **156**, 85–91 (2006).

85. C. Robin et al., *Int. J. Hydrog. Energy*, **40**, 10211–10230 (2015).

86. G. Soubeyran, M. Reytier, F. Micoud, and J.-P. Poirot, *J. Power Sources*, **597**, 234089 (2023).

87. E. Tardy et al., *Int. J. Heat Mass Transf.*, **145**, 118720 (2019).

88. J. Yu, T. Matsuura, Y. Yoshikawa, M. Nazrul Islam, and M. Hori, *Phys Chem Chem Phys*, **7**, 373–378 (2005).

89. E. Endoh, S. Terazono, H. Widjaja, and Y. Takimoto, *Electrochem. Solid-State Lett.*, **7**, A209 (2004).

90. X. Huang et al., *J. Polym. Sci. Part B Polym. Phys.*, **44**, 2346–2357 (2006).

# Advanced methodology for simulating local operating conditions in large fuel cells based on a spatially averaged pseudo-3D model

## Authors

Marine Cornet[1], Jean-Philippe Poirot-Crouvezier[1,z], Pascal Schott[1], Sébastien Kawka[1], Arnaud Morin[1], Yann Bultel[2]

[1]*Univ. Grenoble Alpes, CEA, LITEN, DEHT, 38000 Grenoble, France*

[2]*Univ. Grenoble Alpes, Univ. Savoie Mont Blanc, CNRS, Grenoble INP, LEPMI, 38000 Grenoble, France*

*Corresponding e-mail: jean-philippe.poirot@cea.fr*

*Corresponding postal address: 17 avenue des Martyrs, 38000 Grenoble, France*

# Supplementary Information

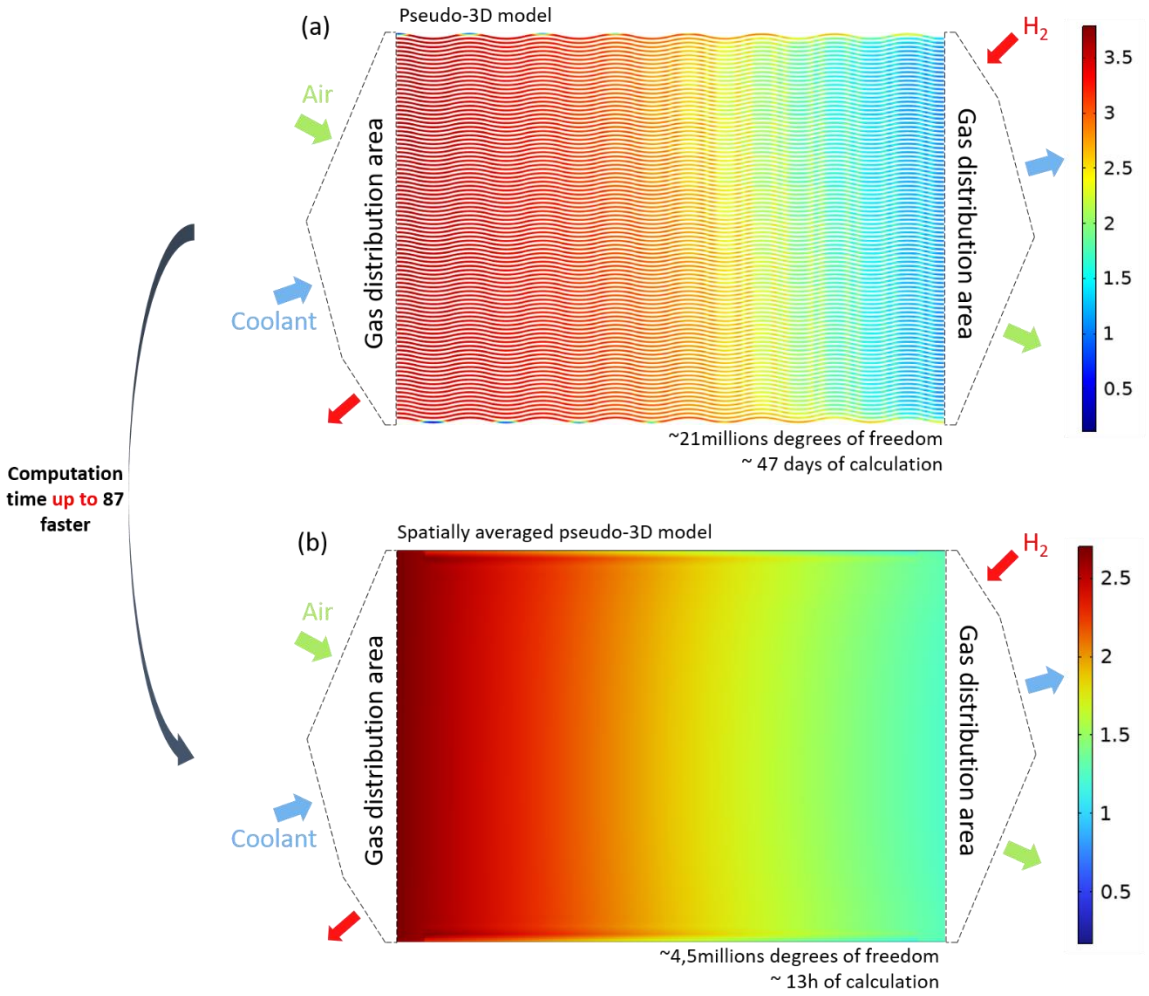


Figure S1: Current density distributions of the P3D model and the spatially averaged P3D model at 1.9 A/cm² (stationary state) 80 °C, 2 bara, 50/60 % RH anode/cathode, 1.5/1.6 stoichiometry anode/cathode **before post-processing**.